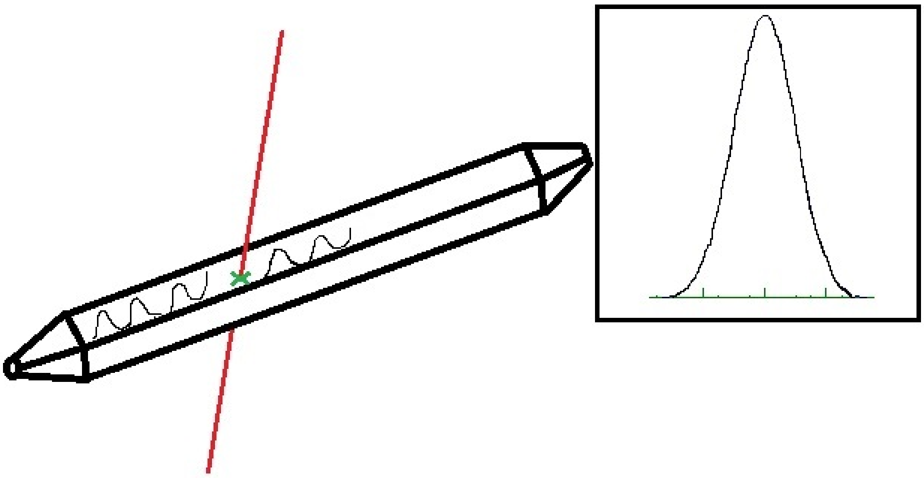

Characterisation of NeuLAND scintillator bars and timing in the S406 experiment.

Master's Thesis in Applied Physics

VEDAD BABIĆ

Department of Fundamental Physics
CHALMERS UNIVERSITY OF TECHNOLOGY
Gothenburg, Sweden 2014
Master's Thesis 2014:1

Abstract

At the R^{3}B (Reactions with Relativistic Radioactive Beams) experiment at FAIR (Facility for Antiproton and Ion Research) studies regarding nuclear structure and dynamics will be performed using exotic nuclei far from stability. One of the main components in the R^{3}B setup is the neutron detector NeuLAND (New Large Area Neutron Detector). A method for the characterisation of plastic scintillator bars for use in NeuLAND involving cosmic muon and LED measurements has been evaluated. The method involves an LED (Light Emitting Diode) as a photon source and a PMT (Photo Multiplier Tube) which are placed on opposite sides of the bar. The attenuation of light intensity from the LED is measured with the PMT simultaneously as cosmic muons impinge on the bar. In order to characterise the bar as having a sufficiently good response, both the cosmic muon and LED response need to be above 90% of the response of a reference bar.

Due to the need of accurate time measurements, two approaches to determine if the walk-effect is present in a time-of-flight wall were considered i.e. if time measurements depend on the energy deposited in the scintillator bar. The first one by analysing data in experiment S406 and extracting the time-of-flights from the start detector, POS to the detector of interest. From this number, a calculated time-of-flight was subtracted. It is seen that there exists an energy dependence on the time measurements and a walk-effect is observed. The observed walk is in the order of several ns. The second approach was to try to determine the walk with the Land02 walk programme which yielded walk curves as well. The walk in this case was in the order of 1-2 ns which agrees with the previous results. An attempt to correct for the walk by approximating the walk function with a linear polynomial did not improve the time measurements.

Acknowledgements

The thesis could not have been finished without the help of so many people which all deserve to be thanked. First and foremost, my supervisor, Andreas Heinz who has helped me throughout the project and provided insightful thoughts and comments on the work. I am grateful to him for pushing me to work and think on my own even when it felt impossible. Secondly I want to thank my partner at the HGS-HIRe Summer Program at GSI, Kazuma Kobayashi for his help and work as well as Igor Gašparić who supervised us for 8 weeks and with whom I later had a lot of discussions regarding experiments and measurements at GSI. I am grateful for the help of Christoph Caesar who supervised us at the summer school in the absence of Igor. I am also grateful to Michael Heil and Konstanze Boretzky from GSI who helped us with our measurements and later with the proof reading of my thesis. I am happy to have been working with Håkan Johansson, Simon Lindberg and Ronja Thies from the Subatomic Physics department at Chalmers, all of whom has helped me with smaller or larger issues as they showed up and always been ready to answer my questions.
Lastly I am thankful to the whole research group at the department of Subatomic Physics, the group meetings were always interesting and the input from everyone was always opening up my view to new and different approaches.

Vedad Babić, Gothenburg 28/4/14

Contents

Part I

Introduction

1

Background

The earlier Aristotelian approach to studying nature was that by changing nature to observe or measure it, we cannot observe its true form, the one which we are interacting with daily. By shattering a glass and examining the pieces, there is no way to learn about the essence of the glass, its shape and volume. Therefore they restricted themselves only to observe and ponder on the nature of things without altering its essence.

With the birth of modern physics and scientists such as Galileo and Newton, measurements and experiments took a special place in physics. It was no longer frowned upon to alter the nature of things to learn more about them, it became the norm.

Although the idea of fundamental particles had already existed for a long time (the idea of there being one undividable particle, the atom), it was not until the early 20th century that the now modern view was formed, with the atom having a positively charged nucleus surrounded by negatively charged electrons which can be excited to higher-lying orbitals.

With new measurements and confirmations, mankind started discovering more particles, such as neutrons, muons, pions and others. Today we have confirmed 17 elementary particles (which do not consist of other particles), 12 fermions (having half-integer spin) and 5 bosons (having integer spin), the latest being the Higgs boson which was recently confirmed at CERN, the European Organization for Nuclear Research in Geneve, Switzerland.

In the field of nuclear physics, the structure of atomic nuclei and nuclear reactions are studied among others. Many exotic nuclei (having a large difference in their number of protons and neutrons) can only be created at accelerators, giving rise to a need of accelerator facilities.

One of these accelerator facilities is GSI (Gesellschaft für Schwerionenforschung) in Darmstadt, Germany. At GSI, ion beams of almost every naturally occurring element, from Hydrogen to Uranium can be generated. This is accomplished by ionizing a sample of the element after which the ions are accelerated either towards a target in which reactions take place or into a storage ring where the beam is circulating.

Currently, the new FAIR (Facility for Antiproton and Ion Research) facility is being constructed at GSI. The two are one; meaning that some of the existing equipment at GSI will be used at FAIR. FAIR will provide antiproton and ion beams of unprecedented intensities, allowing for new insights into the evolution of the universe and the Big Bang, as well as the structure of matter.

To be able to perform accurate measurements and study e.g. nuclear interactions, there is a need for well calibrated detectors with high accuracy. In this thesis we will look at some of the detectors used at GSI in the R^{3}B (Reactions with Relativistic Radioactive Beams) experiment. More specifically we will look at an experiment which took place in November 2012 at GSI, experiment S406, and three detectors in particular. NeuLAND, the new neutron detector, which is under development at GSI and whose prototype was tested during S406, DTF which is a thick time-of-flight wall used for time measurements and the CXB crystal, a NaI crystal from the Crystal Ball (section 3.6) which was used to calibrate the Crystal Ball for proton energies. For NeuLAND a method for characterising the plastic scintillator bars which it consists of has been evaluated. In DTF we have looked at timing, more specifically the walk-effect i.e. if the timing of a signal depends on its amplitude.

2

Thesis outline

The thesis consists of three parts, the first part being an introduction to the R^3B (Reactions with Relativistic Radioactive Beams) experiment at GSI, which includes experiment S406. This experiment lies at the heart of this thesis and will be discussed further in section 3.3. An explanation of the experimental setup is also given, with the detectors and magnets used, as well as a general introduction to scintillation detectors.

The second part describes work on the new neutron detector, NeuLAND (New Large Area Neutron Detector), which is currently under development at GSI, and will consist of 3000 plastic scintillator bars. These bars need to be tested and their quality needs to satisfy the requirements set for the NeuLAND detector in its Technical Design Report (TDR) [1]. A method for testing the bars using a light emitting diode (LED) and cosmic muon measurements is presented[1]. The work presented in this section was partly performed by the author together with a fellow student, Kazuma Kobayashi and partly by researchers in the LAND group at GSI (Konstanze Boretzky, Michael Heil and Igor Gašparić), whose work on section 6.3 and 6.4 is a continuation of the aforementioned measurements and is presented here in order to document it. The simulations mentioned in section 6.4.2 were performed by M. Heil.

In the third and last part, data analysis of the S406 experiment is discussed. More specifically the DTF (German: Dicke Time-of-Flight Wand, English: thick time-of-flight wall) detector and the CXB crystal setup were investigated. In the analysis of the DTF detector, it was tried to establish if there exists a walk-effect i.e. a dependence of time measurements on the amplitude of the signal. In that case, two coincident signals with different amplitudes give rise to two different time measurements, and this needs to be corrected for.

In the CXB, a phenomenon involving protons which seem to traverse the NaI crystal without depositing energy was investigated. It is seen that these protons, which

---

[1] All measurements were performed at GSI where the author spent eight weeks as part of the international summer student program, *HGS-HIRe Summer Student Program at GSI.*

in the data analysis appear to traverse the crystal, in fact did not. They appeared, due to crosstalk in the electronics. That is, the signals resulting from protons traversing nearby detectors were transferred to neighbouring channels through electromagnetic interference, which made it appear as if they traversed the crystal itself.

3

Experimental setup

3.1 Scintillation detectors

The detectors this thesis focuses on, that is the detectors used in experiment S406, are all scintillation detectors. A scintillation detector is a detector which is made from a scintillating material; a material (liquid, gaseous or solid) that emits photons in the visible or near visible range when being struck by a nuclear particle or radiation. The scintillator works by interacting with charged particles and by transforming part of their kinetic energy into optical photons. The created light is detected by a photo multiplier tube (PMT).

Different scintillating materials have different properties, some have faster rise times, meaning a better time resolution while others have higher light output, resulting in a better energy resolution. Currently, there are six types of scintillator materials in use: organic crystals, organic liquids, plastics, inorganic crystals, gases and glasses. Plastics and inorganic crystals are the only ones that will be discussed here as they are the two types of scintillators that were used in experiment S406. Both materials are luminescent, that is they reemit energy in the form of visible light when they are exposed to certain forms of energy, for example light, heat or radiation. But while organic scintillators reemit the light within 10^{-8}s of absorption (the time atomic transitions take is in the order of 10^{-8}s), a process called *flourescence*, the excited state in inorganic crystals is metastable, meaning that the reemission is delayed, a process called *phosphorescence* or *afterglow*.

Plastic scintillators are organic detectors, they consist of solid plastic in which an organic scintillator has been dissolved. They give an extremely fast signal with a decay constant of 2-3 ns and a high light output. Some of the main advantages of plastic scintillators include their flexibility: they can be produced commercially and are easily shaped into desired sizes and forms. They are also relatively cheap. All of the detectors discussed in this chapter are made of plastic scintillators with the exception of the Crystal

Ball and the CXB crystal.

Inorganic crystals are mainly alkali halides which contain a small activator impurity. The most commonly used material (which is also used in the Crystal Ball crystals) is NaI which is activated by Thallium (Tl). Inorganic crystals have in general 2-3 orders of magnitude slower response time (∼500 ns) than organic scintillators. Their advantage lies in their greater stopping power than plastic scintillators due to their higher density and atomic number. In general they also have some of the highest light outputs, which gives a better energy resolution, making them suitable as detectors for γ-rays, high-energy electrons and positrons [2].

When it comes to the S406 detectors, the organic detectors (the ones consisting of plastic scintillator bars), are mostly segmented detectors with horizontal and vertical bars or paddles, except for a few cases. The segmentation allows for, among other things, a better position resolution.

3.1.1 Photo multiplier tubes

Photo multiplier tubes (PMTs) are used to detect photons for time and energy measurements. When the photons reach the PMT, they create electrons via the photo-electric effect by impinging on a cathode made of photosensitive material, a photocathode. Due to the presence of an electric field, the created free electrons are accelerated towards a series of dynodes where each electron produces several secondary electrons, thereby multiplying the number of electrons up to a factor of 10^6 [3]. The electrons are then gathered by an anode from which an electric signal is received, see Figure 3.1. The signal amplitude depends on the intensity of the incoming photons.

3.1.2 Interaction of γ-rays with matter

Due to γ-rays having a large part in the measurements conducted in this thesis (crystal ball being a γ detector and having performed LED measurements in Part II of the thesis), a short introduction of how γ particles interact with matter is of importance.

The behaviour of photons in matter is limited to three different kinds of interaction: photoelectric absorption, Compton scattering and pair production. At low γ-energies, the photoelectric effect is prevalent and at high γ-energies, pair production is the main interaction type. At medium energies (the exact quantitative value depends on material type, mostly the nuclear charge of the absorber), Compton scattering is the most common interaction type[2].

To measure γ-ray energies correctly, they need to deposit all of their energy in the detector. This is the case in pair production (where the photon transforms into an electron-positron pair) and photoelectric absorption where a bound electron absorbs the photon and is ejected from the atom. In both cases it is easy to detect the electron due to the high stopping power of the scintillator. The positron is also easily stopped but it is annihilated, creating two 511 keV photons which in turn also need to be detected to measure the total energy of the initial γ. Interaction by Compton scattering does not

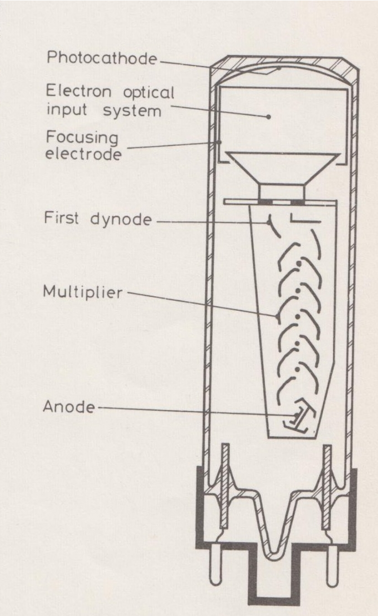

Figure 3.1: A schematic drawing of a photomultiplier tube. Figure from Ref. [2].

deposit all of its energy, thus making photoelectric absorption the easiest case in which the energy of the incoming γ-ray is measured.

3.2 R^{3}B experiment

At the R^{3}B (Reactions with Relativistic Radioactive Beams) experiment at FAIR [4], studies regarding nuclear structure and dynamics will be performed using exotic nuclei far from stability. With the R^{3}B experimental setup it will be possible to do kinematically complete measurements of the reactions i.e. to identify all outgoing particles and fragments and to measure their four-vectors. It will be possible to perform experiments with stable and unstable beams at beam energies ranging from 150 MeV/u up to 1.5 GeV/u and to study e.g. nuclear structure, reaction mechanisms and fission of radioactive isotopes [5].

The benefits of using relativistic beam energies include the possibility of quantitative descriptions of reaction mechanisms together with other experimental merits, such as the usage of relatively thick targets (in the order of 1 g/cm^2). Due to the beam being relativistic, having a high velocity, there will be a forward focusing of the reaction products due to the Lorentz boost, allowing for full-acceptance measurements with moderately sized detectors [6].

Radioactive beams at high energies are used to study the properties of atomic nuclei far from stability by impinging them on a fixed target. These reactions have permitted, among others, the extraction of detailed spectroscopic data which is weakly influenced by reaction mechanisms. GSI is currently the only accelerator facility in the world in which experiments with stable or radioactive beams up to ^{238}U with energies up to 1 GeV/u can be performed [5].

The experimental configuration will be based on the current R^{3}B/LAND setup but will provide improvements in the energy resolution, particle identification, and detection efficiency. In Figure 3.2 the future R^{3}B experimental setup can be seen. The R^{3}B collaboration is an international collaboration consisting of members from more than 50 different institutes located all over the world.

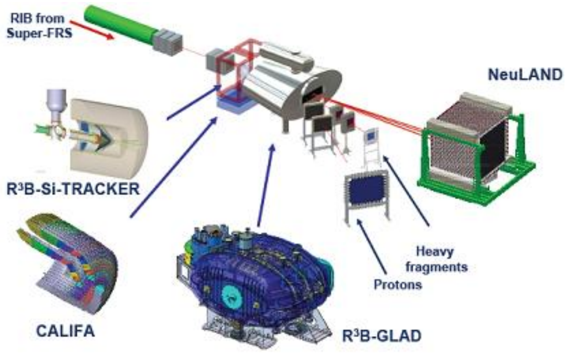

Figure 3.2: The first phase of the future R^{3}B experimental setup with the main components - gamma and proton detector CALIFA, silicon tracker, superconducting magnet GLAD, detectors for charged particles after the magnet and neutron detector NeuLAND. In the second phase a high-resolution spectrometer will be added.

3.3 S406 experiment

The aim of the S406 experiment which was performed in November 2012 at GSI was to test the response of different detectors to fast neutrons. This was achieved with a deuteron beam impinging on a CH_2 target, producing 'monoenergetic' neutrons from quasifree breakup. The proton in the deuteron scatters against a proton in CH_2. Both protons from this (p,2p) reaction can be detected with the Crystal Ball detector allowing to trigger on this reaction channel.

One aim was to characterise a NeuLAND (New Large Area Neutron Detector, a neutron detector consisting of plastic scintillator bars) prototype in order to verify technical solutions outlined in its technical design report (TDR) [1] as well as studying its detection efficiency and time resolution [7].

The technical design report (TDR) defines the design requirements for NeuLAND, not only in terms of physics (time and momentum resolution, etc.) but it also includes details of the technical realization, mechanics, read-out electronics, calibration and construction procedures.

The experiment was not only focused on NeuLAND, but its progenitor LAND (Large Area Neutron Detector) as well, which stems from 1990, but which has as of lately been equipped with new electronics (TacQuila) recquiring a new characterisation.

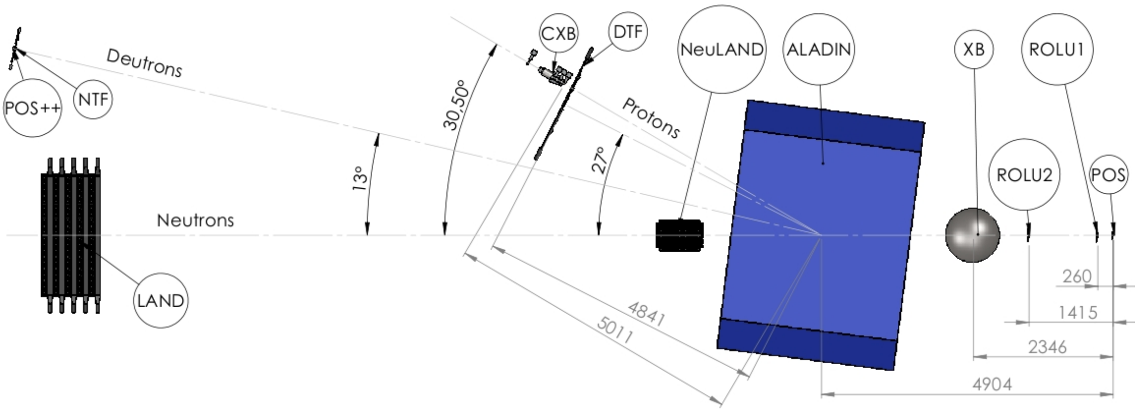

Figure 3.3: Schematic drawing of the S406 experimental setup. Figure from Ref. [8].

The setup can be seen in Figure 3.3. The deuteron beam energies ranged from 200 MeV/u to 1500 MeV/u. The reaction target is placed inside the Crystal Ball in a target frame. In experiment S406 measurements were performed with a C or CH_2 target or with an empty target frame for background measurements [9].

3.4 POS detector

The POS detector is used as a start (or stop) detector for time-of-flight measurements in experiments. It defines the start time of the particles impinging on it. Normally, POS is a quadratic plastic scintillator (5.5x5.5 cm^2), which is connected to four photomultiplier tubes on each side, see Figure 3.4. In S406, a plastic scintillator with a size of (length x width x thickness) 10x2x2 cm^3 was used instead. This change was made due to the beam which consisted of deuterons which have a low atomic number, Z. Low-Z particles deposit a lower amount of energy[1] and require a thicker detector. A thicker detector produces larger light output and better resolution, but it also gathers more background data, e.g. from cosmic particles which are created in the atmosphere. Due to this, the thickness was kept as low as possible while preserving a time resolution below 100 ps. The acronym POS comes from its earlier use as a position sensitive detector, as which it is no longer used.

In S406, two identical POS detectors were in use, POS and POS++, as can be seen in Figure 3.3. The POS detector served as a start detector for a time-of-flight measurement and was placed horizontally perpendicular to the beam direction, in front of the target and the POS++ detector, which was placed at the back next to the NTF (New Time-of-Flight wall) detector, was positioned vertically. Both detectors are read out by two

---

[1] The energy loss of a charged particle in matter follows the Bethe-Bloch formula, which states that $-\frac{dE}{dx} \propto Z^2$.

photomultipliers on the opposite sides of the detector.

The POS++ detector was used to determine the time resolution of the POS detector. This was achieved by measuring the time distribution between the two detectors. The time-of-flight measurement is given by the following equation:

$$T = \frac{t_1(POS++) + t_2(POS++)}{2} - \frac{t_1(POS) + t_2(POS)}{2} \tag{3.1}$$

where $\mathrm{t_i}$ is the time measured by the different PMTs. The width of the time distribution is given by

$$\sigma = \sqrt{\sigma_{POS}^2 + \sigma_{POS++}^2} = \sqrt{2}\sigma_{POS} \tag{3.2}$$

The last equation is given by the fact that POS++ is constructed identical to POS ($\sigma_{POS} = \sigma_{POS++}$).

With this method the time resolution of the POS detector can be calculated ($\sigma_{POS} = \sigma/\sqrt{2}$).[10]

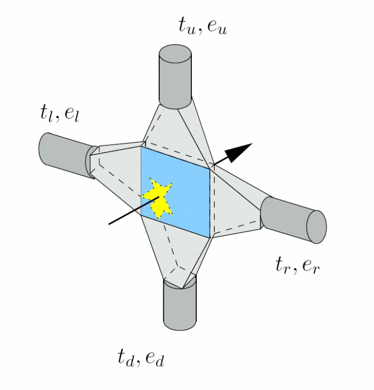

Figure 3.4: A schematic drawing of the POS detector. In the picture the quadratic plastic scintillator is seen together with the four connected PMTs. In S406, a 10x2x2cm^3 plastic scintillator was used instead, with only two PMTs connected on opposite sides.

3.5 ROLU detectors

In S406, two ROLU detectors were in use. The detectors consist of four movable plastic scintillators ('Rechts', 'Oben', 'Links', 'Unten' or Right, Up, Left, Down in English) and are used to define the accepted beam spot size. Any particle impinging on any of the scintillators will create a signal that may be used as veto for the beam trigger, that is, when analyzing the data one may discard all the events where a particle hit any of the ROLU scintillators. In S406, the dimensions of the scintillators were 95x100x10 mm^3. In Figure 3.5 the design of the detectors can be seen [11].

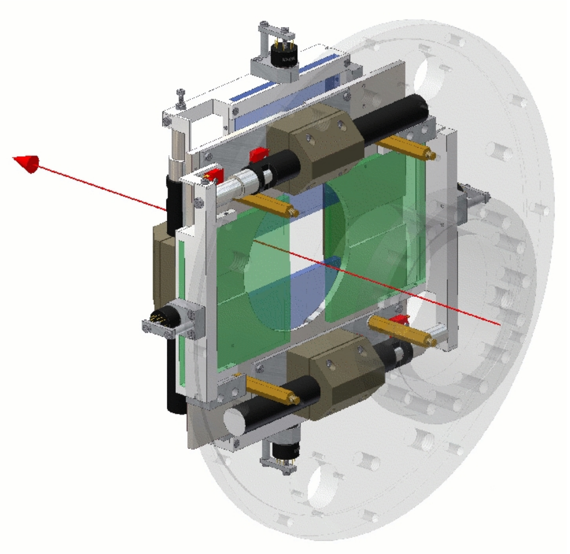

Figure 3.5: A schematic drawing of the ROLU detector. The blue and green plastic scintillators can be seen together with their respective direction of motion. The red line shows the beam direction.

3.6 Crystal Ball detector

The main objective of the Crystal Ball is to detect the multiplicity and energies of γ-rays and protons emitted in the reactions taking place in the target, which it encloses. It consists of 162 NaI crystals in a 4π setup. The crystals are activated with Tl creating a scintillating material. Crystal Ball has a spherical shape with an inner radius of 25 cm and an outer radius of 45 cm. Each crystal covers a solid angle of 77 msr and, to achieve equal coverage, four different shapes (called A, B, C and D) of crystals are used, a regular pentagon (12 crystals) and three kinds of irregular hexagons (60+60+30 crystals), see Figure 3.6 [11].
Each of the 162 crystals has an individual label, a number ranging from 1 to 162. They are placed so that the sum of two opposing crystals is always 163. The two crystals in the beam direction, crystal 81 and 82 (81+82=163) are removed during experiments as to not interfere with the beam pipe, as well as crystal 77 which is on the bottom, so that the target can be supported mechanically [8].

Initially, the Crystal Ball was intended for studying nuclei at high angular momenta by detecting the total energy and multiplicity of the emitted γ-rays from a collision process. The γ-ray energies detected were typically around 0.1-3 MeV [13]. As a high energy γ and proton-spectrometer was needed at GSI within the R^3B experiment, the Crystal Ball was used. Although it was initially designed to detect photons of lower energies, it proved to be well-suited for the detection of high energy protons (several hundred MeV) thanks to the high stopping power of the NaI crystals while also detecting

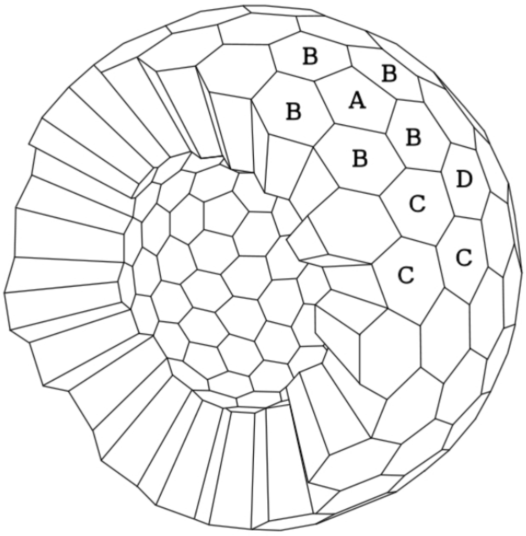

Figure 3.6: The crystals building up the Crystal Ball, the different letters show the different shapes of the crystals. Figure from Ref. [12].

the high energy γ-rays (20-30 MeV) efficiently. Although an installation of low-gain amplifiers were needed for the detection of high energy protons (see section 3.6.1). Due to the high granularity of the Crystal Ball, individual particles and their paths are measured. When γ-rays are emitted from reacting nuclei, their energy is *Doppler shifted* when measured in the detector. This Doppler shift depends on the angle which it makes with the beam and needs to be corrected for[2]. With a larger granularity, the individual crystals cover a smaller range of angles, giving a smaller spread in the Doppler shifted energies in each crystal [14].

3.6.1 Electronics of the Crystal Ball

To detect high-energy photons and protons, the Crystal Ball needed to be calibrated. When particles traverse the crystal, photons are created which are detected in the PMT. The number of photons created depend on the particles' charge and energy.

The protons have a higher energy deposition than γ-rays, resulting in larger signals from the PMT. Since both protons and γ-rays should be detected in the Crystal Ball, an extra PMT low gain output was installed in the forward hemisphere, due to the forward focusing of the reaction products in a collision at relativistic beam energies. Having installed an extra PMT output, two signals were received from each PMT, one from the photocathode and one from a dynode before, which has a lower gain. The reason for

---

[2] The detected (or shifted) energy (E_S) for a photon with velocity v, angle θ and 'unshifted' energy E_0 is: $E_S = E_0(1 + \frac{v}{c}cos(\theta)$

not using only one output is that the electronics which integrate the signals only work in a certain energy range (it only has a certain number of channels available). If it is calibrated for energies typical for the γ-rays, it means that the protons will produce saturated signals (all the signals with amplitudes above a certain value yield the same result). On the other hand if only the low gain output is used, the lower energies will be squeezed to a a few channels giving a low energy resolution for γ-rays.

3.7 ALADIN magnet

ALADIN (A Large Acceptance DIpole magNet) is a dipole magnet with a large gap placed after the crystal ball. The amount of deflection that the magnet imposes on a charged particle is given by its magnetic rigidity:

$$B\rho = \frac{m_0 c\beta\gamma}{qe} \tag{3.3}$$

where B is the magnetic field, ρ is the bending radius of the particle due to the magnetic field, $\gamma = (1-\beta^2)^{-1/2}$ is the Lorentz factor, $\beta = \frac{v}{c}$ the velocity of the particle, m_0 its rest mass and q its charge. It can be seen that for a given magnetic field, the bending radius depends on the momentum and charge of the particle. In this way it is possible to distinguish different particles by measuring their deflection angles.

Because of the relativistic beam energy the reaction products are kinematically focused in forward direction. To measure as many particles as possible, having a large acceptance helps. The size of the ALADIN gap is 1.5x0.5 m^2 [15]. The magnet is placed such that it deflects protons and other charged particles towards the two time-of-flight walls (detectors used for time-of-flight measurements) DTF and NTF while neutrons keep travelling in an unchanged direction towards the neutron detectors LAND (Large Area Neutron Detector) and NeuLAND (New Large Area Neutron Detector).

3.8 Neutron detector NeuLAND

NeuLAND [1] is the successor of the LAND and will be used to detect fast neutrons with kinetic energies from 10 MeV to 1.5 GeV [4] [16]. It consists of plastic scintillator bars (5 cm x 5 cm x (250 cm + 10 cm of light guide on each side)) in a setup where the bars are mounted in planes. Neighbouring planes have mutually perpendicular bars. The light guides are made of the same material as the bar and have a conical shape. The full setup will consist of 3000 plastic scintillator bars placed in 30 double planes, where each double plane holds 50 vertical and 50 horizontal bars, see Figure 3.7. It will be possible to split NeuLAND into two independent detectors for special applications.

NeuLAND will provide a momentum resolution, Δp/p of 10^{-3} which requires a time-of-flight resolution of σ(t) $<$ 150 ps and position resolution of σ(x,y,z)$\approx$ 1.5 cm. In addition it will have enhanced capability for identifying neutron multiplicity

The NeuLAND prototype that was used in S406 consisted of 150 plastic scintillator bars which were placed vertically in a setup with 15x10 scintillator bars [9].

Figure 3.7: One of the NeuLAND double planes mounted with 100 bars. Behind the vertical bars 50 horizontal bars are mounted.

3.9 Time-of-flight wall DTF

DTF is a thick time-of-flight wall which was used for detecting protons in S406. It was therefore placed at a large angle, 27° with respect to the ALADIN magnet. The DTF consisted of 6 vertical and 2 horizontal plastic scintillator bars. The dimensions of the vertical bars are 20x120x1.5 cm^3 while the horizontal ones measured 10.4x140x1 cm^3 [11] [16], see Figure 3.8. The reason for using thick bars is the need to detect light charged particles which do not deposit a lot of energy.

3.10 CXB crystal and detector setup

The CXB setup is not part of the earlier mentioned R^3B/LAND setup, it was included in the setup to resolve questions concerning the energy calibration of Crystal Ball for high energy protons. The setup was placed behind DTF (Figure 3.3) at a 30° angle with respect to the ALADIN magnet. Due to the large angle, protons were impinging on the DTF and subsequently also the CXB crystal. The Crystal Ball is initially a γ-detector which was later upgraded with a high-energy electronic branch (section 3.6) to detect protons. The energy deposited by high energy protons had to be correlated to the energy deposited by cosmic muons which are used for the energy calibration. This was to be achieved with the CXB setup, which consists of six plastic scintillators placed around a Crystal Ball crystal, see Figure 3.9. The design of the detector setup is based

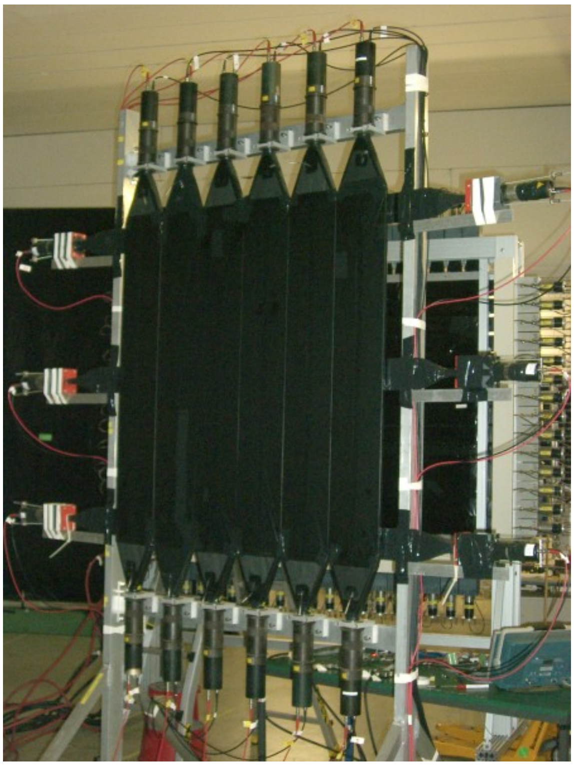

Figure 3.8: A picture of the DTF-detector. In this case the DTF has three horizontal bars. In S406, the central bar was removed, leaving it with two horizontal bars.

on simulations performed at Chalmers in 2012 as a part of a Bachelor thesis [17].

The idea of the setup is that a cosmic muon hits one of the plastic scintillators, travels through the crystal and then hits another plastic scintillator on the way out. In this way a well-defined path length through the crystal is achieved leading to a well-defined energy loss. With this path length the absolute energy deposition can be calculated, due to cosmic muons being minimum ionizing particles (thus their energy loss being dependant only on the path travelled, not on their incident energy) and an energy calibration can be achieved. Protons, unlike cosmic muons, are not minimum ionizing particles, meaning that their energy deposition is not linearly dependant on their path travelled through the crystal. This means that, unless the proton is fully stopped in the crystal, only a part of their energy is detected. The measured energy varies with the energy of the proton; a higher initial energy results in a lower measured energy deposition. To calibrate the energy deposited by the protons, it is possible to analyse data when the protons are fully stopped in the crystal and correlate the energy measured with the energy deposited by cosmic muons. This then allows the calibration of the full Crystal Ball with cosmic muons for these energies.

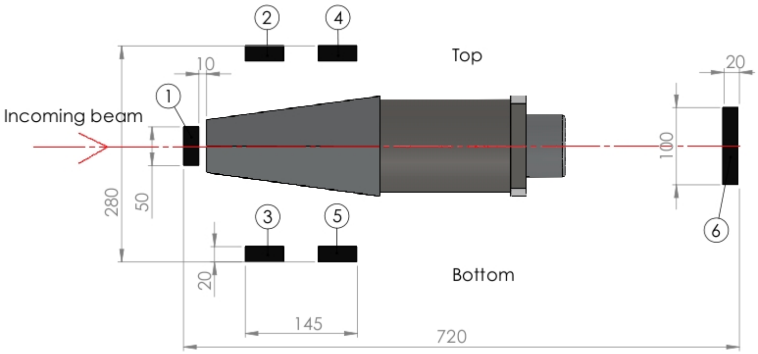

Figure 3.9: The CXB setup during the S406 experiment. The CXB crystal has been placed behind the fifth vertical bar of the DTF.

3.11 Neutron detector LAND

LAND (Large Area Neutron Detector) is used for the detection of fast neutrons (energies >150 MeV). It covers an area of 2x2 m^2 and has a depth of 1 m, see Figure 3.10. It has ten planes each of which consists of 20 plastic scintillator bars (200 in total). The detection method is based on converting the neutrons into protons via nuclear reactions in iron layers, the protons are in turn detected by the plastic scintillators. Between each plane of scintillator bars there are 11 sheets of iron (5 mm thick except for the two outer layers which have a thickness of 2.5 mm) with 10 sheets of scintillator material (5 mm thick) between each sheet of Fe (Figure 3.11) [11]. Each plane of scintillator bars is perpendicular to the plane in front and behind of it.

3.12 NTF

The detection principle of the NTF (New Time-of-Flight wall) is similar to that of the DTF. It consists of 8x8 plastic scintillator bars with dimensions of 480x60x5 mm^3. It is used as a detector for fast-moving-fragments produced in reactions in the target. Light ions are deflected more in the ALADIN magnet and impinge on the DTF detector, heavier reaction products are deflected less and are detected by the NTF [11].

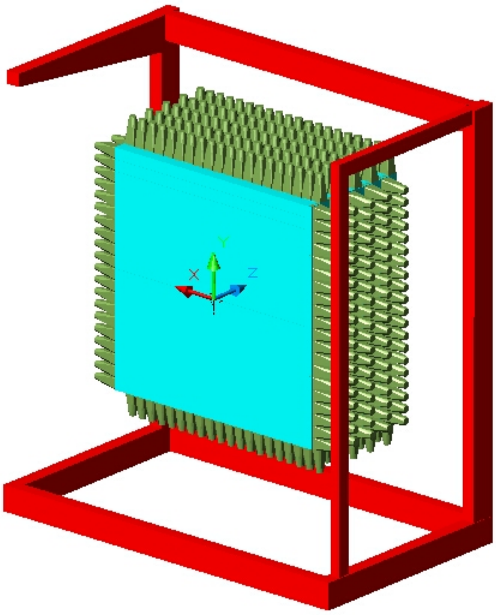

Figure 3.10: A sketch of the LAND detector. One can see the 10 planes with bars perpendicular to the planes in front and back of them.

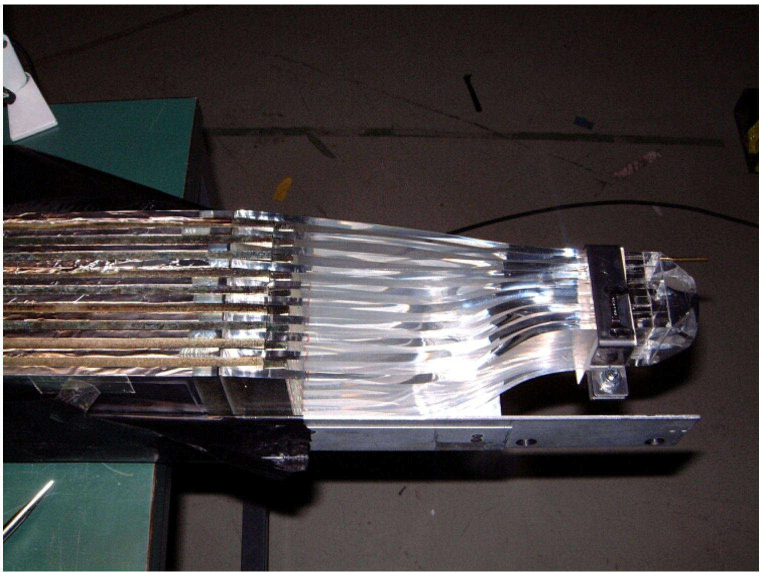

Figure 3.11: The photo shows the eleven iron sheets with scintillator material in between which are placed between each plane of scintillator bars.

Part II

Characterisation of NeuLAND bars

4

Introduction: Characterisation of NeuLAND bars

NeuLAND will consist of 3000 plastic scintillator bars measuring 270x5x5 cm^3, including a 10 cm light guide on each side of the bar. The light guides are of the same material as the bar and have a conical shape. The bars and the light guides are wrapped in reflector foil and black tape to prevent environmental light from entering the bar as well as keeping the light created inside the bar from escaping. They need to satisfy the requirements set in the technical design report (TDR) for NeuLAND. Thus a procedure for quick testing of bars was established involving an LED (Light Emitting Diode) and cosmic muon measurements.

Initially three plastic scintillator bars were ordered from the company REXON Components Inc. in the USA. These three bars showed good performance with respect to the light output, satisfying the design goals of NeuLAND. New bars which were produced afterwards had lower quality and in case they do not meet the requirement of having a light output of at least 90% of one of the initial bars (from now on referred to as *standard bars*), they need to be sent back to REXON for exchange. During the project, 100 bars from the latest delivery (July and August 2013) were tested, each bar being given a number from 1-100 to be able to distinguish them. In order to examine the quality of the bars in more detail, attenuation length measurements with cosmic muons were attempted.

4.1 Electronics

As described earlier the scintillation light signals are read out by PMTs at the ends of the bars. The PMT signals are sent to the electronics card TacQuila [18], developed at GSI. It contains a discriminator, a TDC (time-to-digital converter) and a QDC (charge-to-digital converter). The discriminator receives a signal, which for a signal amplitude

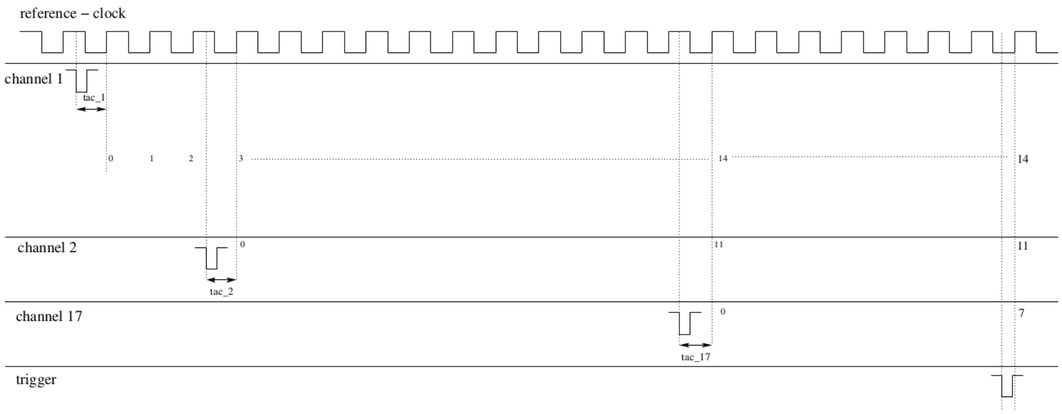

Figure 4.1: The TacQuila timing is shown. It has 17 channels, out of which 16 are used as input channels for signals while the 17^{th} is used as a stop signal. It uses a 40 MHz external clock to measure the time between input signal and the stop signal (or rather; it counts the number of clock cycles that are performed by the clock), see the text for further information. Figure from Ref. [18].

over a certain value, creates a *logic 1* signal as an output. This is important to, for example, obtain time measurements of signals. Since there is always electronic noise (e.g. due to reflections in cables) there needs to be a criterion by which a *real* signal created by the interaction of a particle or radiation in a detector can be distinguished from noise. Different types of discriminators deal with this problem in different ways, two of which are discussed in chapter 10.

The TacQuila data is read out by the GSI DAQ (Data AcQuisition) system MBS (Multi Branch System) running on a RIO3 processor which can be accessed via the ethernet. The DAQ stores the collected data as list-mode data, which means that the data is stored event-by-event. The decision to store information about a certain event is made by the DAQ trigger, after which the data is collected and digitised at the same time.

The TacQuila card has 17 channels, 16 of them are used as input channels for signals while the 17^{th} is used as stop signal. The incoming signals are split into two chains; a timing chain and an energy chain. In the timing chain the signal is discriminated and sent to the TDC as a start signal (defining the start time), where a 40 MHz external clock is used. The TacQuila measures the time until the rising edge of the next clock signal, t(tac$_i$) for channel i, after which a clock counter starts counting clock cycles. This counter is counting until a trigger signal from the DAQ is received (in channel 17, which will also count the time until the next rising edge provided by the clock, t(tac$_{17}$), see Figure 4.1. The time can then be determined using the following equation:

$$t_i = t(tac_i) - t(tac_{17}) + \frac{counter_i}{clockfrequency} \tag{4.1}$$

The energy signal is integrated in the QDC. The QDC pedestals (zero-energy offsets) were measured and subtracted. In the analysis no absolute energy calibration was needed, therefore all energies are given in channel numbers unless stated otherwise.

4.2 Light intensity attenuation measurements

The idea of using LED measurements to test the quality of the scintillation bars is based on the fact that particles traversing the bars produce photons. These photons travel through the bar and reach the PMTs where they are collected, which allows for light attenuation measurements. The advantage of LED measurements compared to cosmic muon measurements is the possibility of using a high frequency pulser; the LED measurements in this section used a 10 kHz pulse frequency. This can be compared to the average cosmic muon flux at sea level which is in the order of 1 muon/cm^2/min [19]. A rough estimate gives a flux in the order of 10 muons/s impinging on the bar[1] which is a difference of three orders of magnitude. The photons from the LED traverse the whole length of the bar since the PMT and LED are placed on opposite sides, the cosmic muons on the other hand impinge at any position along the bar. In the latter case, a position calibration of the interaction point is needed to determine where the cosmic muons impinged on the bar. This can be achieved by measurements with two PMTs on opposite sides of the bar and a collimated γ-source. By placing the γ-source at different well-defined positions along the bar, the time difference of the resulting measurements can be calibrated to give position information.

Both the PMT and the LED are placed in a holder which was designed to fit to the light guide of the bar. A piece of black textile is inserted between the light guide and the holder to prevent environmental light from entering the PMT, see Figure 4.2. When a different bar is to be measured, the PMT and LED holders are dismounted and mounted on the next bar.

4.3 Method

In this section, three different types of measurements are discussed, LED measurements, cosmic muon measurements and measurements with a collimated γ-source. In the former case, an LED and a PMT are placed on opposite sides of a bar while in the two latter cases two PMTs are placed on opposite sides of the bar, see Figure 6.1.

In the LED measurements, the LED[2] emits photon pulses with a certain frequency and intensity during a specific amount of time. The photon pulses traverse the whole length of the scintillation bar before being detected by the PMT. In the cosmic muon case, photons are created when the muons pass the scintillator bar and are detected in the PMTs. By measuring the time difference of the two PMT signals resulting from a muon traversing the bar, the interaction point of the muon with the bar can be calculated.

---

[1] The top area of a bar is 270x5 = 1350 cm^2. Since the bar is not a two-dimensional object, the muon rate in the bar is higher due to the possibility of impinging on the sides, meaning that the flux is higher than 1350 muons/min (22.5 muons/s). At lower zenith angles, the flux decreases [20], meaning that including the whole bar does not change order of magnitude of the flux.

[2] The LED is of type ChipLED 0402, emitting photons with a wavelength of λ=466 nm.

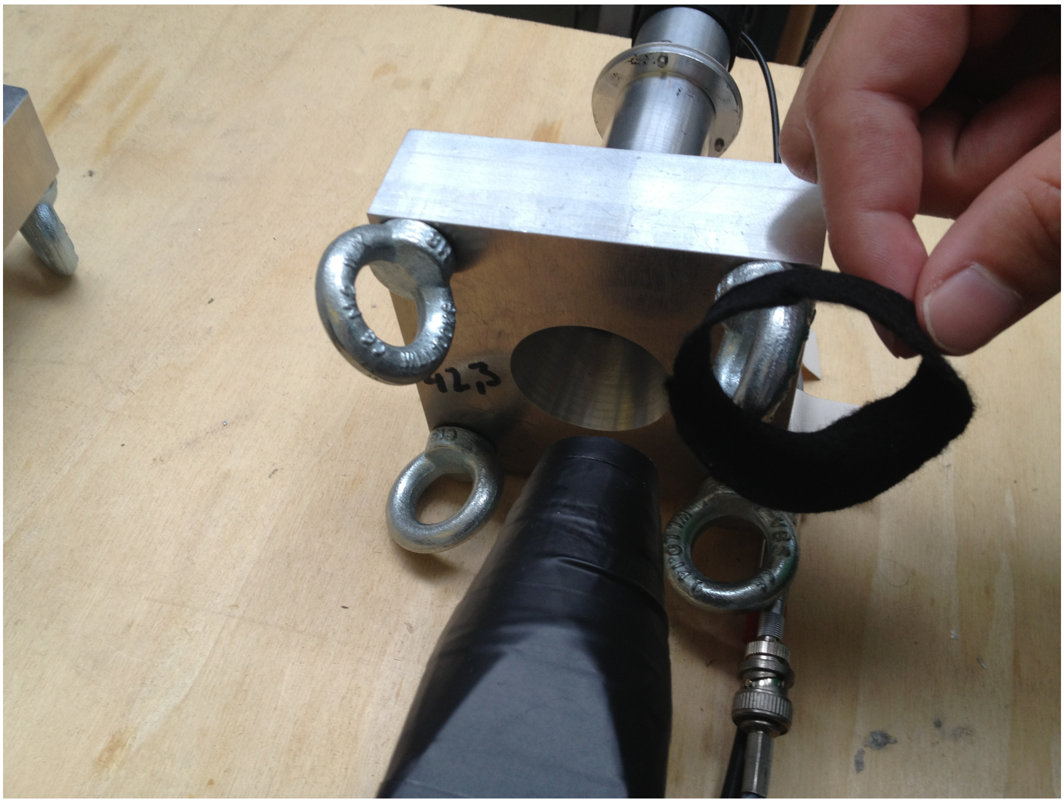

Figure 4.2: Bar together with the holder that goes on the light guide and a textile which is placed on the light guide to prevent environmental light from entering the PMT.

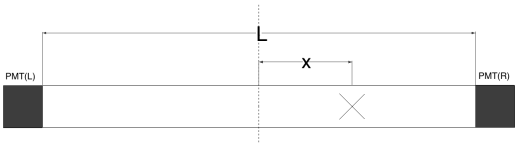

Figure 4.3: A schematic figure of a bar of length L with two PMTs mounted on opposite sides. The interaction point of a particle with the bar, ×, is measured with respect to the center of the bar (x∈[-L/2,L/2]).

The amplitude of this signal is ideally linearly dependent on the incoming light intensity. The result of such a measurement is a histogram of the number of incoming photons. This histogram is fitted to a gaussian (see Figure 4.4) and provides a mean value, μ_{gauss} and a standard deviation, σ_{gauss}.

4.3.1 Attenuation of light intensity

Photons traverse the plastic scintillator during all of the measurements mentioned. In the case of LED measurements, photons emitted by the LED traverse the whole bar

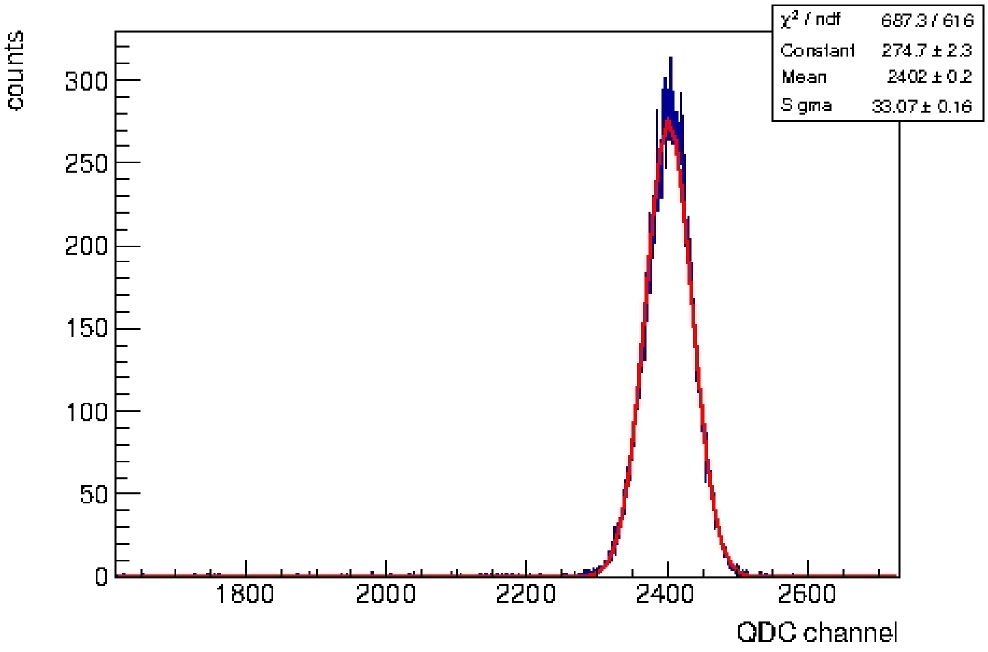

Figure 4.4: An example of a measurement with a LED where the resulting energy histogram has been fitted to a gaussian function.

length while the traversed length of photons created by the cosmic muons depends on the interaction point. In all cases, the light intensity decreases exponentially as photons traverse matter. The decrease is characterised by the attenuation length of the material, λ:

$$I(x) = I_0 e^{-x/\lambda} \tag{4.2}$$

where x is the length traversed and I_0 the initial intensity.

In all LED measurements, I_0 is a constant determined by the output of the LED. The gaussian fit of the measured energy spectrum gives the mean light intensity after having traversed the whole bar length. The resulting value of μ_{gauss} is related to the light intensity measured by the PMT. A higher value of μ_{gauss} implies less attenuation of the light intensity.

4.3.2 LED measurements

The LED measurements were conducted in cycles. For example, i bars are measured in N cycles. A cycle constitutes measurements of all the bars once, one after the other in an ordered manner. Between each measurement, the measured bar is dismounted and the next one mounted. In each measurement, a $\mu_{gauss,bar,cycle}$ and a $\sigma_{gauss,bar,cycle}$ value is obtained by fitting the resulting spectrum to a gaussian function. The duration of each measurement is the same in all measurements.

From the cycle measurements, a mean value of all the $\mu_{gauss,bar,cycle}$ values is calculated relative to the standard bar (stdbar):

$$\mu^*_{bar} = \frac{1}{N} \sum_{cycle=1}^{N} \frac{\mu_{gauss,bar,cycle}}{\mu_{gauss,stdbar,cycle}} \tag{4.3}$$

where N is the number of cycles. The mean value over all cycles, which is not relative to the standard bar, is simply denoted as μ_{bar}.

The standard deviation of μ_{bar} is also calculated:

$$\sigma_{bar} = \sqrt{\frac{1}{N} \sum_{cycle=1}^{N} (\mu_{gauss,bar,cycle} - \mu_{bar})^2} \tag{4.4}$$

The value of $\sigma_{mean} = \sigma_{bar}/\mu_{bar}$ is used to determine if the spread of the measurements is sufficiently low. Since it is always used in the context of measurements of a single bar, the bar-index is dropped in the following. The aim for σ_{mean} was to be around 1%[3] at worst.

---

[3] The value was chosen to ensure that the measurements are reproducible and the measured attenuation of light intensity is in agreement with the requirements set by the NeuLAND TDR.

5

Testing the method

First, the stability of the method had to be tested i.e. if the measurements are reproducible given that the bar needs to be mounted and dismounted between each measurement. Three different bars were used, the standard bar, bar 5 and bar 15. The measurements were performed so that first the standard bar was measured, then bar 15 and lastly bar 5. This procedure was conducted for 10 cycles. Each measurement lasted approximately 10 seconds. The measurements were unstable with a σ_{mean} of around 5%, see Table 5.1.

Due to the large variation in the results between the measurements (large value of σ_{mean}), a longer, ten minute measurement was performed (the time span over which the shorter measurements were performed was in the order of ten minutes). If the fluctuations originated from the electronics, they should also be present in the longer measurement, unless the problem magically disappeared. In that case the width, σ_{gauss} would be larger compared to the shorter measurements. The longer measurement resulted in approximately the same μ_{gauss} as the shorter measurements (2250 versus 2274) and the same width, σ_{gauss} (33.2 versus 32.5) (see Table 5.2), which means that the fluctuations had most probably a different origin, perhaps the mounting and dismounting of the bar. In that case there are a couple of possible sources for the fluctuations; the mounting and dismounting of the PMT or LED or maybe the textile placed in between the holder and the light guide allows the holders to move around between the measurements or doesn't keep environmental light from entering the PMT. In the first case, the PMT (or LED) can be taped to the bar to ensure that it does not move and perform measurements where the LED (or PMT) is mounted and dismounted between each measurement. In the case of the textile, the textile can be rotated between the measurements to see if it has any impact on the results. By changing the textile to a slightly different one, the influence of the size of the textile on the results can be investigated.

Table 5.1: The results from ten cycles of measurements of the three bars. The deviation around or above 5% is far from satisfying. It is desirable to have a deviation around 1%.

Bar	Mean Value [ch]	σ_{mean} (%)
Standard Bar	2274.22	6.26
Bar 5	2196.58	6.12
Bar 15	1617.92	4.34

Table 5.2: The result from the longer 10 min control measurement compared to the previous measurements from Table 5.1. The values presented are mean values over the ten measurement cycles.

Bar	Mean Value [ch]	σ_{gauss} [ch]
Standard Bar (10 min meas.)	2250.0	33.2
Standard Bar (shorter meas.)	2274.22	32.5

5.1 PMT measurements

To try to establish if the PMT was the cause of the high σ_{mean} values, the LED holder was taped onto the bar (Figure 5.1) so that it could not move as the PMT was mounted or dismounted. Ten measurements taking around ten seconds each were performed. All measurements except one gave consistent results. Together the σ_{mean} was 6.5% but without the deviating measurement, under the assumption that it is faulty, the σ_{mean} value is 2.5% which is still not satisfactory, see Table 5.3.

5.2 New PMT

PMTs have a so called μ-metal which shields them from the influence of external electromagnetic fields. The first PMT that was used had a visible external μ-metal, in contrast to an integrated one, which is placed around it. This made the diameter of the PMT larger and prevented the usage of an o-ring for stabilization within the PMT holder, allowing it to move around. A Si-pad was inserted between the scintillator and PMT to remove air that might exist at the interface between the PMT and the scintillator, thus reducing reflections by the introduction of a layer with an index of refraction which lies in between the values of the two neighbouring materials.

Given that the PMT resolution was insufficient to accomplish the desired width (σ_{mean} around or less than 1%), it was decided to replace the PMT with another one, which had an integrated μ-metal so that an o-ring could be used to stabilise it in the holder. A Si-pad covering the front of the PMT was not used. Because the bar was mounted and dismounted frequently one assumption was that it might get dirty in the

Table 5.3: The results from ten cycles of measurements of bar 5 with the LED taped to the light guide. The results were not satisfying. The 2^{nd} measurement deviated more than the others. Even removing it from the data set, under the assumption that it is faulty, does not result in a satisfying width.

Mean Value [ch]	σ_{mean} (%)	Comments
3906	6.5	All meas.
3985	2.5	All except 2^{nd} meas.

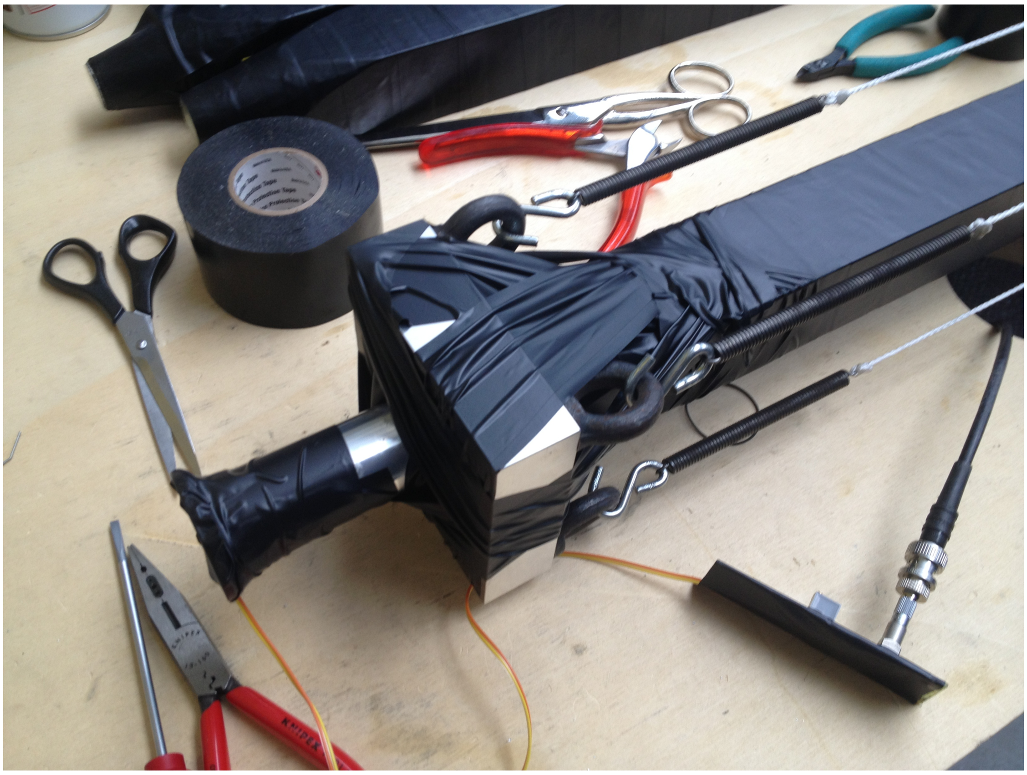

Figure 5.1: The LED taped to the bar to prevent movement.

process, causing the measurements to become unreliable as time progresses.

The LED, which was initially placed at the back of the holder, was now taped to a PMT which is placed inside the holder. In this way the distance between the LED and the light guide is minimised.

Ten consecutive measurements were taken with the same bar where the new PMT was mounted and dismounted in between. The results were stable with a σ_{mean} value of 1.04%, compared to the earlier value of 6.5%. The conclusion drawn was that the o-ring stabilises the PMT. The LED which was now placed closer to the bar also allowed for more precise measurements to take place.

5.3 Impact of the textile

The next five measurements were dedicated to check the impact of the textile on the measurements. The reason for this was that depending on the shape of the textile, it may change the distance between the LED to the bar and affect the number of photons passing the scintillator bar. When the textile was changed to a different one, the results were very consistent but with a lower recorded mean channel, μ_{gauss} (3256 versus 3985) which confirmed the hypothesis that the textile had an influence on the measurements.

To make sure that the placement of the textile during the mounting/dismounting procedure does not produce large fluctuations in the measurements, five measurements were performed where the textile was rotated after the PMT holder was dismounted. The results were once again very stable with a σ_{mean} value of 0.92%.

5.4 LED mounting/dismounting measurements

The stability of the measurements with respect to the LED mounting and dismounting procedure was also tested. The PMT was fixed by taping it to the bar, and ten measurements were performed where the LED was mounted and dismounted in between. Once again, the measurements lasted around ten seconds each and resulted in a σ_{mean} value of 0.6%. This means that the method where an LED emits photons on one side of the bar, which traverse the bar is stable with respect to the mounting and dismounting procedure of the equipment and reproducible results can be expected.

5.5 Measurements of all the bars

As both the LED and PMT measurements were stable with respect to the mounting and dismounting of the bars, measurements of the 100 bars were performed, in cycles where the standard bar was first measured followed by measurements of several ($\sim$10) bars before the standard bar was measured once again. All bars demonstrating a value of μ^*_{bar} above 92% were classified as satisfactory and no further measurements were performed on them. The rest of the bars went through further tests of similar kind in three cycles.

The results of the measurements are presented in Figure 5.2 and show a disagreement with the data which was received from REXON, the company that produced the measured scintillator bars. The method used by REXON to perform their measurements is proprietary and has therefore not been observed by any researcher from GSI but REXON has explained that they made measurements similar to those performed at GSI. In later discussions with the company, information has surfaced that their LED has been emitting too high light intensity, leading to saturation in the PMT, which is why the results do not vary a lot.

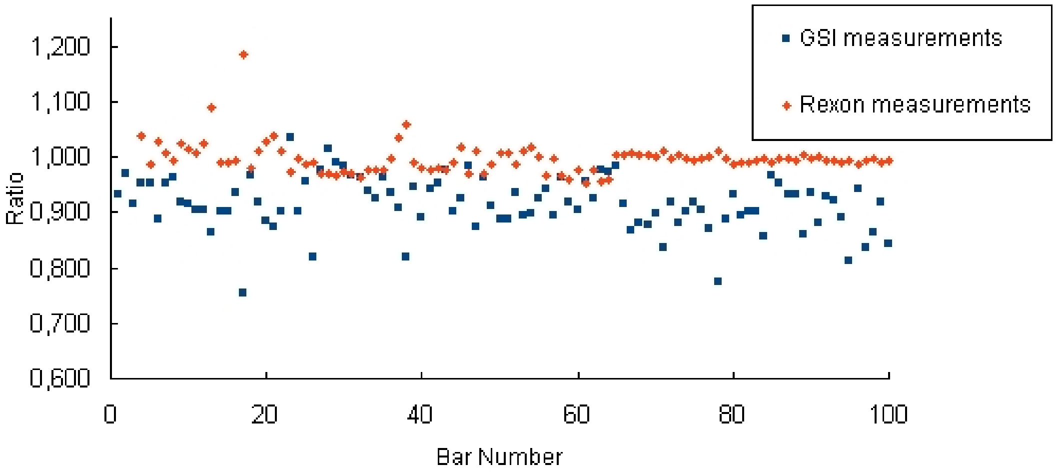

Figure 5.2: μ^*_{bar} plotted versus bar number. The results from the LED measurements of the bars, together with the data of the bars supplied from REXON.

6

Measurements with cosmic muons and a γ-source

In order to confirm the results of the LED measurements, the attenuation length of the bars has been measured with cosmic muons. To perform the measurements, it is necessary to know where on the bar the cosmic muons impinge, determining the distance light travels before entering the PMTs. The measurements are performed with two PMTs mounted on opposite sides of a bar. By measuring the time difference of the two PMT signals resulting from a muon traversing the bar, the position of the interaction of the muon with the scintillator can be calculated. The calibration of the time difference to position is performed with a ^{22}Na γ-source. The source is placed at well-defined positions along the bar and collimated to ensure that the γ-rays impinge the bar at the specific positions. The ratio between the interaction point position and the time difference is the effective velocity of light in the bars, and is assumed to be the same in all bars since they are made of the same material.

For two PMTs located at the left and right ends of a bar (Figure 6.1), the measured times and energies can be described by the following equations:

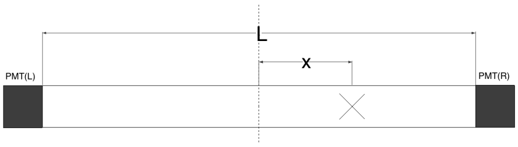

Figure 6.1: A schematic figure of a bar of length L with two PMTs mounted on opposite sides. The interaction point of a particle with the bar, ×, is measured with respect to the center of the bar (x∈[-L/2,L/2]).

$$\begin{aligned} t_L =& \frac{1}{v_{eff}}\left(\frac{L}{2}+x\right)+T \\ t_R =& \frac{1}{v_{eff}}\left(\frac{L}{2}-x\right)+T \\ E_L =& \qquad Ee^{-\frac{(\frac{L}{2}+x)}{\lambda}} \\ E_R =& \qquad Ee^{-\frac{(\frac{L}{2}-x)}{\lambda}} \end{aligned} \tag{6.1}$$

where v_{eff} is the velocity of light in the scintillator material, L is the length of the bar, x represents the position of the interaction in the bar, T is the interaction time, E is proportional to the deposited energy at the interaction point, and λ is the attenuation length of the scintillator material. The time of the interaction and the value of the deposited energy at the interaction point are calculated with the following equations:

$$\begin{aligned} T =& \frac{t_L-t_R}{2}-\frac{L}{2v_{eff}} \\ E =& \sqrt{E_L E_R}e^{-\frac{L}{2\lambda}} \end{aligned} \tag{6.2}$$

Finally, the interaction position can be reconstructed using equation 6.1. It can be determined either from time or energy signals:

$$\begin{aligned} x =& \frac{v_{eff}}{2}(t_L-t_R) \\ x =& \quad -\frac{\lambda}{2}(\ln\frac{E_L}{E_R}) \end{aligned} \tag{6.3}$$

6.1 Calibration of the effective velocity of light in the bars

The setup consisted of one scintillator bar and two PMTs located at the ends of the bar. Gamma-source measurements were performed with a collimated ^{22}Na source placed at different positions along the bar (six measurements in steps of 40 cm). The time-difference spectrum shows peaks which correspond to different positions of the source (Figure 6.2). The peaks lie on top of a background spectrum (mainly due to ^{40}K but also other particles [21]) which can be determined by measurements without the source and has to be subtracted to obtain clean signals. The γ-source measurements may also be used to determine the attenuation length, using the second equation of equation 6.3 (see Figure 6.3), although this is very time-consuming to do for more than one bar, which is why muons are used instead. The effective velocity of light in the scintillators can be calculated with the first equation in equation 6.3.

The effective velocity of light in the bars, i.e. the conversion factor between the time difference (in ns) and position (in cm) is obtained by analyzing the γ source measurements. As a result of this time calibration, the effective light velocity in the scintillator is determined to be v_{eff} =14.74±0.3 cm/ns.

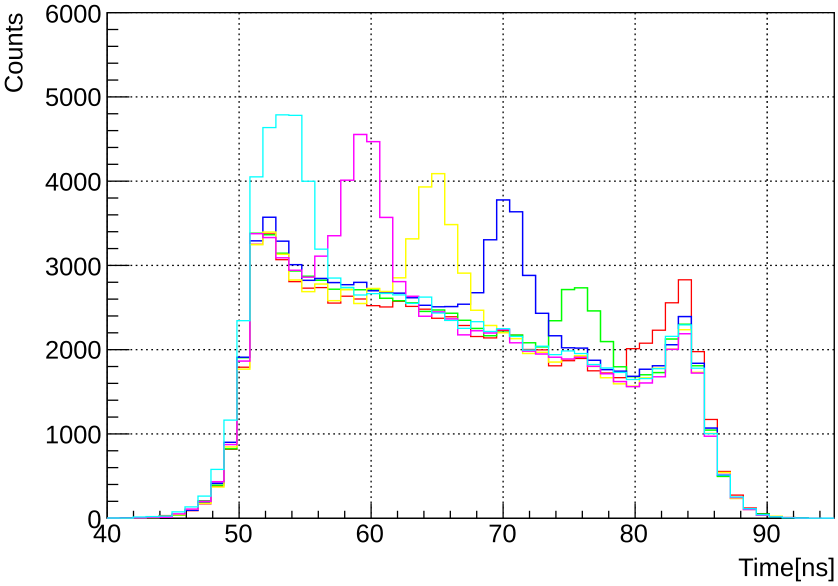

Figure 6.2: A time histogram from the source runs. Each peak is 40 cm apart from the next. Position measured from the time difference is effective for calculating the attenuation length.

6.2 Attenuation measurements with cosmic muons

The attenuation length λ is given as the slope of equation 6.3 and extracted from a fit of the data shown in Figure 6.3. The result from the γ measurements is 330±1 cm.

The cosmic muon measurement of the attenuation length (Figure 6.4) for the standard bar is 474±1 cm. The attenuation lengths of several bars were measured and the relative attenuation over the full length of the bar relative to the standard bar is evaluated. The results from the cosmic muon measurements are plotted together with the LED attenuation measurements for the same bars in Figure 6.5.

The difference in results between the cosmic muon measurements and the γ-source measurements might be due to the difference in the deposited energy. The cosmic muons, depositing much more energy, produce significantly more photons than the γ-source. Due to PMT non-linearity (meaning that the PMT output is not linear with respect to the incoming light intensity), different results are obtained. To determine if this is indeed the cause, muon measurements with different gains on the PMTs were performed by changing the PMT bias voltage. The following two sections deal with investigating non-linearities in the electronics and absolute attenuation length measurements, respectively. The non-linearities need to be investigated to allow for correct LED and cosmic muon attenuation measurements.

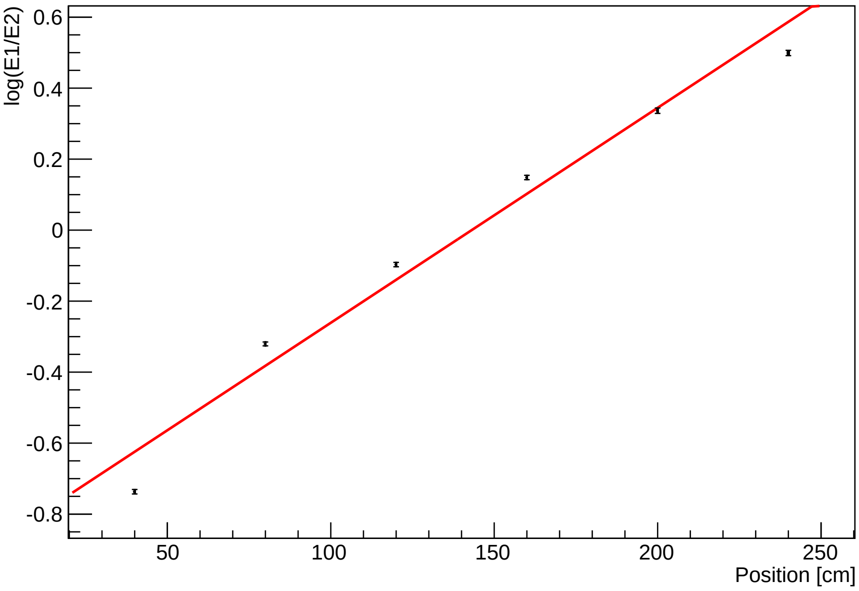

Figure 6.3: ln(E_L/E_R) plotted against the interaction point along the bar for the source measurements. The different symbols correspond to the different positions at which the source measurements were performed. The slope gives the attenuation length.

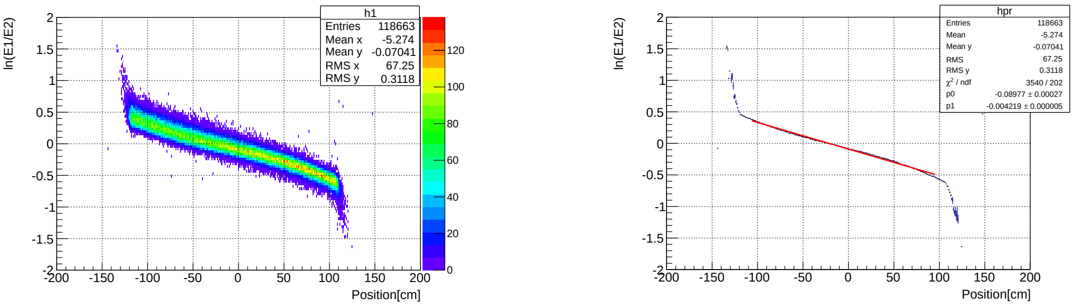

(a) **(b)**

Figure 6.4: (a) Plot of $\ln(\frac{E1}{E2})$ against position of the cosmic-muon hits. (b) Scatter plot of the earlier data and a fit with a linear function.

6.3 Non-linearities in the electronics

By changing the high voltage (HV) of the PMTs (changing the gain) it can be seen that the applied HV affects the attenuation length measurements with cosmic muons, see Figure 6.6. A suggestion is that this dependence arises from non-linearities in the PMT. To determine if this is the case, also QDC non-linearity was investigated.

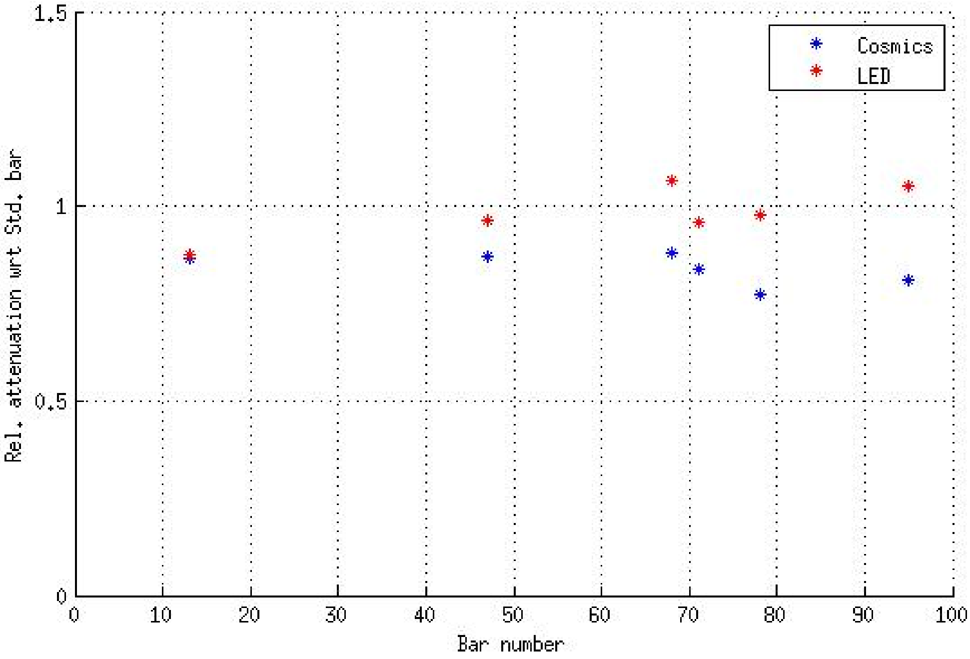

Figure 6.5: The mean value μ^*_{bar} for different bars, both from LED and cosmic muon measurements.

6.3.1 Non-linearity in the TacQuila QDC

By measuring the input signal to the QDC with an oscilloscope, it can be seen that the QDC output value is not linearly dependent on the charge of the incoming signal, as is expected, see Figure 6.7.

To obtain the charge, the QDC output channel was corrected with the following equation:

$$Q(x) = 9 * 10^{-6}x^2 + 0.0285x \tag{6.4}$$

where x is the original channel output supplied from the QDC.

6.3.2 PMT non-linearity

Having confirmed and corrected for QDC non-linearity by correcting the QDC output, the existence of PMT non-linearity was investigated. The non-linear behaviour is assumed to follow:

$$NL(x) \propto \frac{x}{1+kx} \tag{6.5}$$

where *NL(x)* is the non-linear output value from the PMT, x is the light falling on the PMT and k is a non-linearity constant.

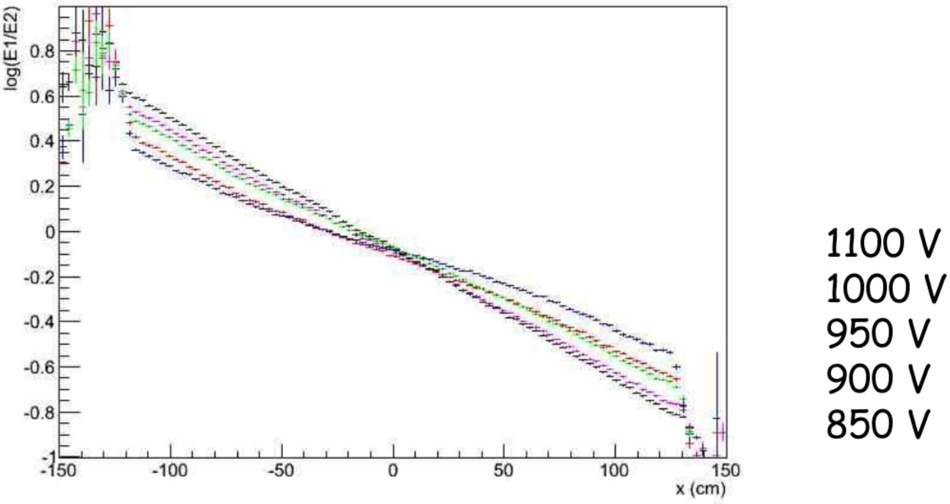

Figure 6.6: $ln(E_1/E_2)$ plotted as function of the position of the interaction point for different HV on the PMTs. The slope changes for different applied bias, suggesting that the PMT response is not linear.

The QDC output as a function of the incoming PMT signal amplitude is shown in Figure 6.8.

The charge of the PMT signal (from equation 6.4) is measured as a function of the incoming LED light intensity. The idea is that the light intensity decreases with the distance squared. The result of the measurements are shown in Figure 6.7 with the fits to the ideal inverse square law and to the saturation formula (6.5).

6.3.3 Measurements with two PMTs

The PMT saturation can be studied with two PMTs where one PMT serves as a reference. The light intensity was measured simultaneously with the two PMTs while varying the emitted LED intensity, see Figure 6.8. The two PMTs were placed at different distances from the LED. The result of the measurements is given in Figure 6.9 where the two integrated PMT signals (given by the Tacquila QDC corrected for non-linearity in equation 6.4) are plotted against each other. Given that the PMTs have a linear response in both PMTs. This would lead to straight lines in the figure, which can not be observed in these measurements. The conclusion is that there are non-linearities in the PMTs, which can be avoided by lowering the bias of the PMTs. This is supported by the fact that the lines are straight at low bias, meaning that the output is linear up until a certain point where the non-linearities appear.

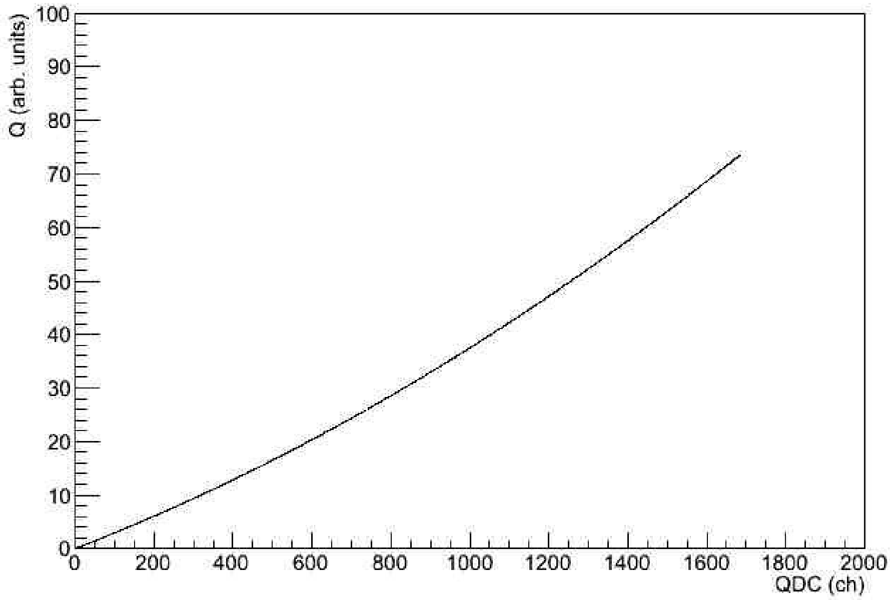

Figure 6.7: Incoming charge versus charge measured by QDC . It is seen that the digitized charge does not depend linearly on the charge at the QDC input.

6.4 Attenuation length measurements

To determine the absolute attenuation length of the bars, the reflections of the light on different surfaces inside the bars needs to be taken into account for. In this chapter an attenuation model including these reflections will be introduced and a determination of the attenuation length is attempted.

6.4.1 Reflections at the PMT

By observing PMT traces on the oscilloscope, signal reflections can be identified originating, presumabely from the light guide-PMT interface and the surface of the conical-shaped light guide (Figure 6.13(b)). To include such reflections into the attenuation length determination, an attenuation model including a reflection constant, α, was used:

$$E_{L,R} = (1-\alpha)E_0 e^{-\frac{L/2\pm x}{\lambda}} + \alpha E_0 e^{-\frac{L/2\mp x}{\lambda}} e^{-L/\lambda} \tag{6.6}$$

where E_0 is the deposited energy. Equation 6.6 can be rewritten to:

$$E_{L,R} = E_0 e^{-L/2\lambda}[e^{\mp x/\lambda} + \alpha(e^{\pm x/\lambda}e^{-L/\lambda} - e^{\mp x/\lambda})] \tag{6.7}$$

To obtain a cleaner spectrum, four NeuLAND bars were stacked on top of each other

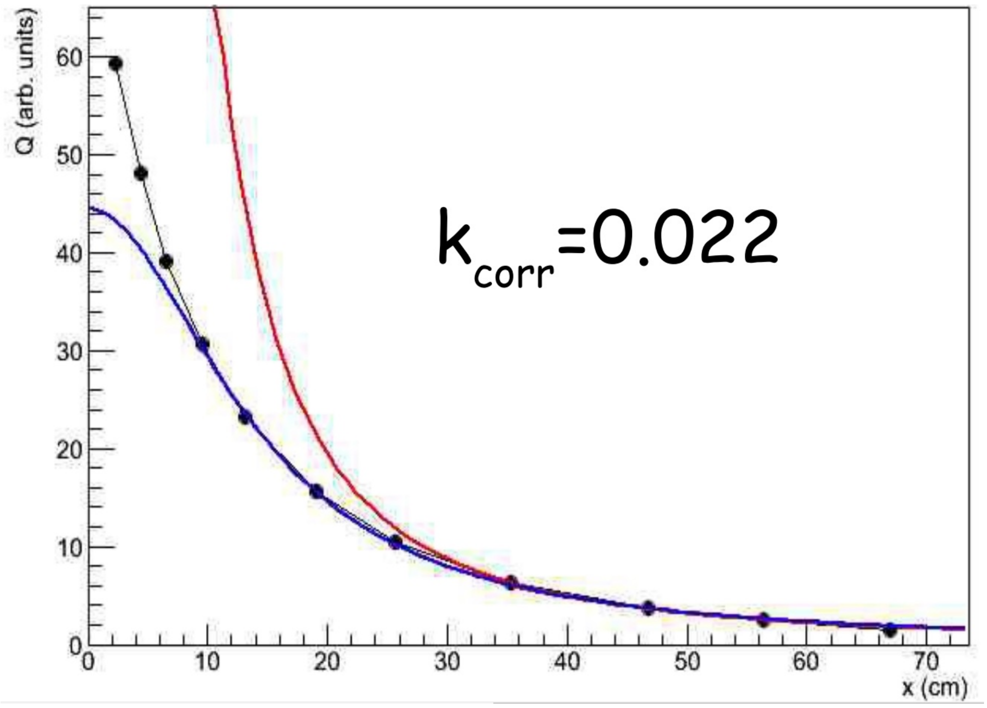

Figure 6.8: Dotted line: incoming charge charge into the QDC versus the distance between the PMT and the LED. The blue line is a fit of the data to equation 6.5. The non-linearity constant is k=0.022. The red line shows a fit of the data with the ideal case, when the intensity drops with distance squared. The red line is a good fit for lower intensities or smaller signals while taking non-linearities into account gives overall a better fit even for larger signals.

for cosmic muon measurements, see Figure 6.11. By doing this a 'cut'[1] or decision can be made to analyse only data where cosmic muons have traversed all four bars. This way it is possible to avoid events where muons hit the sides of the bar.

Although the attenuation length can be calculated using equation 6.7, the value of α has to be known. One option is to fit equation 6.7 to experimental data from the four stacked bar measurements but many different values of α are received from the fit depending on the chosen fit window, see Figure 6.12.

---

[1] In discussions regarding data analysis, a term that is often used is 'cut' or 'cuts'. When applying a 'cut' to a set of data, a choice is made to exclude (or include) certain events. For example, a cut can be made on the particle energy to analyse only events where the incoming particles' energies are in a certain energy range. Cuts can be made on energies (see former example), times (particles having a certain time-of-flight), detectors (particles must or must not have traversed a certain detector) and so on.

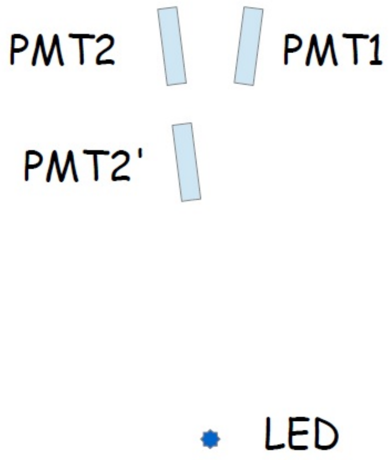

Figure 6.9: The setup with two PMTs and a LED. The light intensity decreases with the distance squared. If the relative distance between the two PMTs is known, the relative light intensity reaching each PMT can be calculated. The distance can be changed by placing PMT2 at position PMT2' instead.

6.4.2 Simulations of the reflections

To try to understand the reflections better, light propagation in the a bar was simulated. The simulations were made in a C++ toolkit called Geant4, which was developed at CERN (European Organization for Nuclear Research) for 'simulating the passage of particles through matter'. Although it was developed for making accurate simulations of particle detectors, applications range from medicine to astrophysics [22].

The bar was reconstructed in Geant4, and a photon source was simulated at one end of the bar. At the other end the number of photons is recorded. The simulations show that the reflections that were seen on the oscilloscope did not arise from interface between light guide and PMT, which are negligible, but rather from the light guide itself (Figure 6.13). Photon sources were simulated along the bar and a determination of the attenuation length was attempted. In this case the photon number was recorded at both ends of the bar.

The smiley effect

The measured energy in the bar is given by the two lower equations in equation 6.1. Multiplying the two equations with each other and taking the square root gives the second equation in equation 6.2. This equation is independent of the interaction point position of the particles. A plot of this value from a previous experiment at GSI from the LAND detector can be seen in Figure 6.15. This plot shows a position dependence of $\sqrt{E_L E_R}$. The effect of a position dependence on $\sqrt{E_L E_R}$ is called the smiley effect. This must mean that the signal attenuation can not be completely described by equation 6.1.

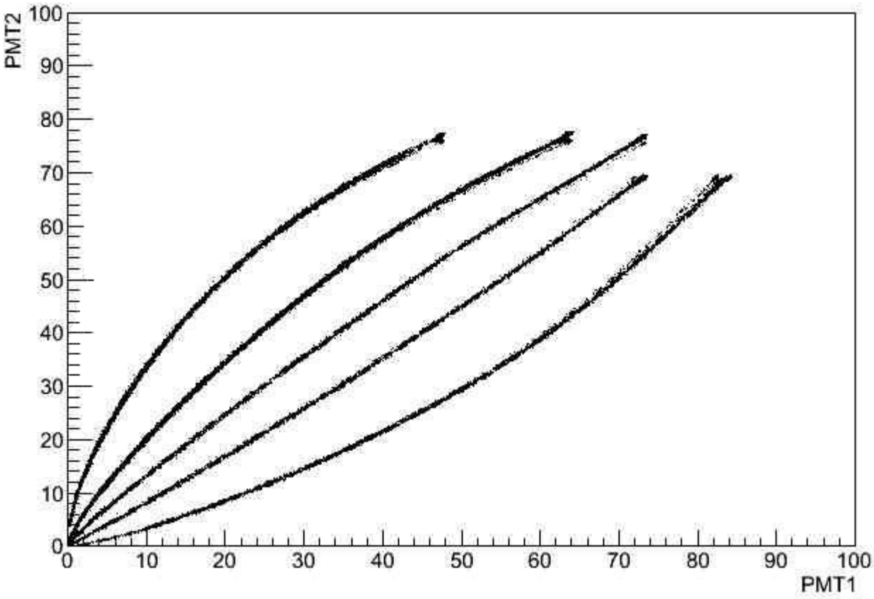

Figure 6.10: The integrated charge from two PMTs plotted against each other after the QDC non-linearity has been corrected for. The positions of the LED with respect to the two PMTs (PMT2, PMT1), is given from the left in cm: (68,31), (68,51), (51,51), (51,68), (31,68)

Another important fact is that not much of the light created in the bar travels directly to the PMT. There are reflections at the surface of the bar and possibly at the interface between PMT and light guide (which is discussed in the previous section) [8]. The Geant4 simulations show that there should be a very slight smiley effect in the NeuLAND bars, see Figure 6.16. The cosmic muon measurements with four stacked bars do not show any clear smiley effect, see Figure 6.14.

Due to the presence of two free paramenters, the attenuation length λ and the reflectivity α, it is not possible to determine both of them at the same time from equation 6.6. One of the two needs to be determined by other measurements.Suggestions include trying to measure the reflectivity using an oscilloscope to get an objective value or to consciously decide a value for the reflectivity to be able to compare attenuation lengths to each other without having an absolute measurement. The former is preferred.

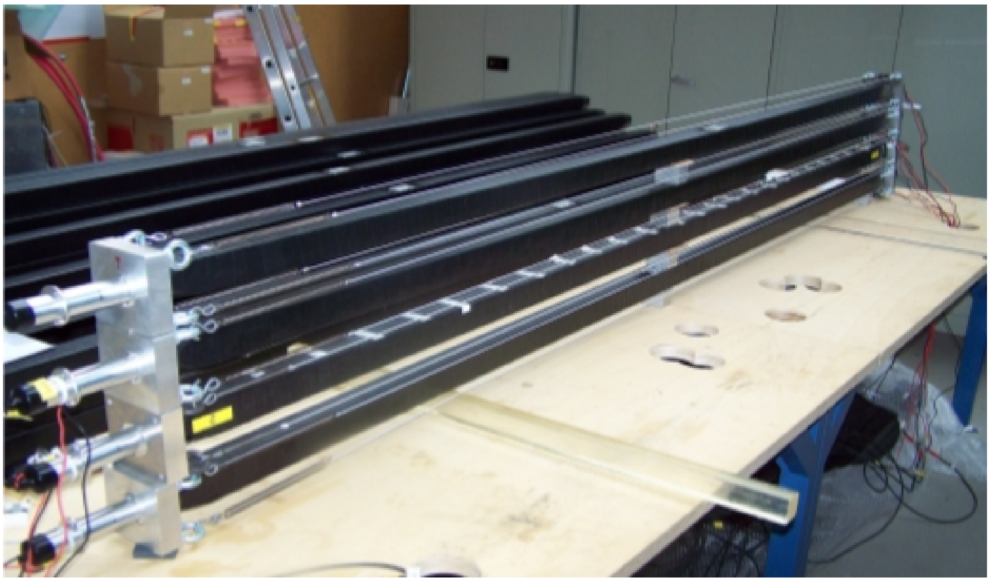

Figure 6.11: The setup consisting of four bars stacked on top of each other to obtain cleaner, better defined hits, allowing to cut on events where the muon passed through all four bars.

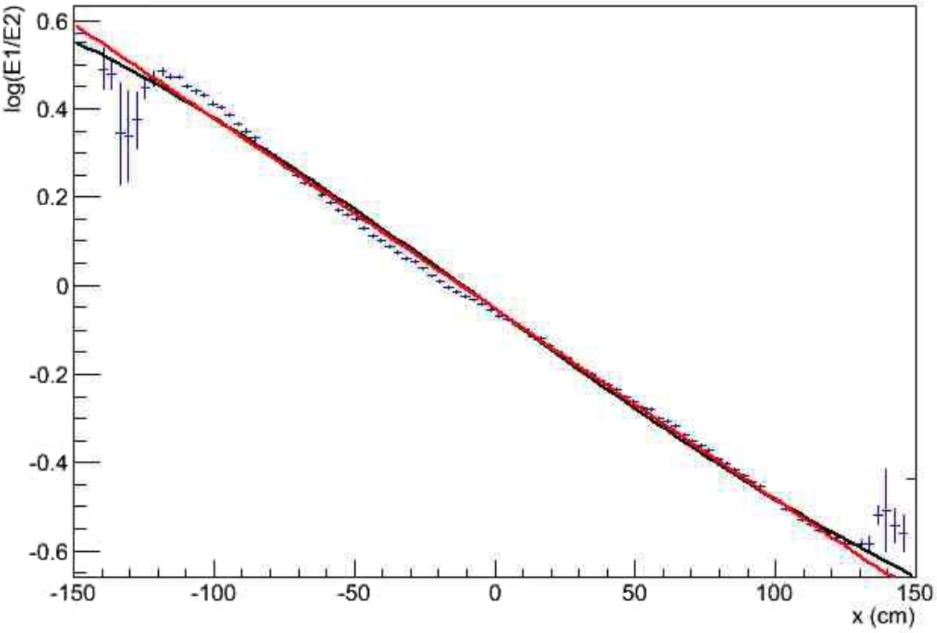

Figure 6.12: $ln(E_L/E_R)$ vs position on the bar. The slope gives the attenuation length. Two fits can be seen, one with a reflectivity, α = 56% leading to an attenuation length of 210 cm and α = 8% giving an attenuation length of 420 cm. Both fit the data well.

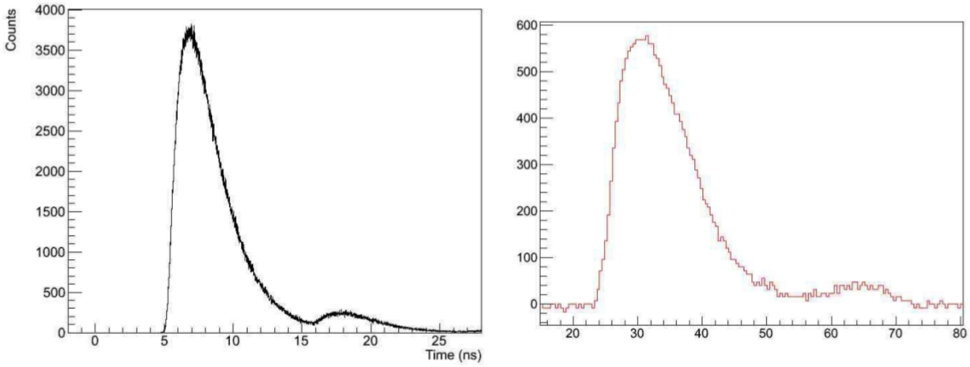

Figure 6.13: (a) The simulated PMT signal and (b) the experimental signal. In both cases the lagging peak is caused by reflections. Both figures have approximately the same shape and show the same behaviour.

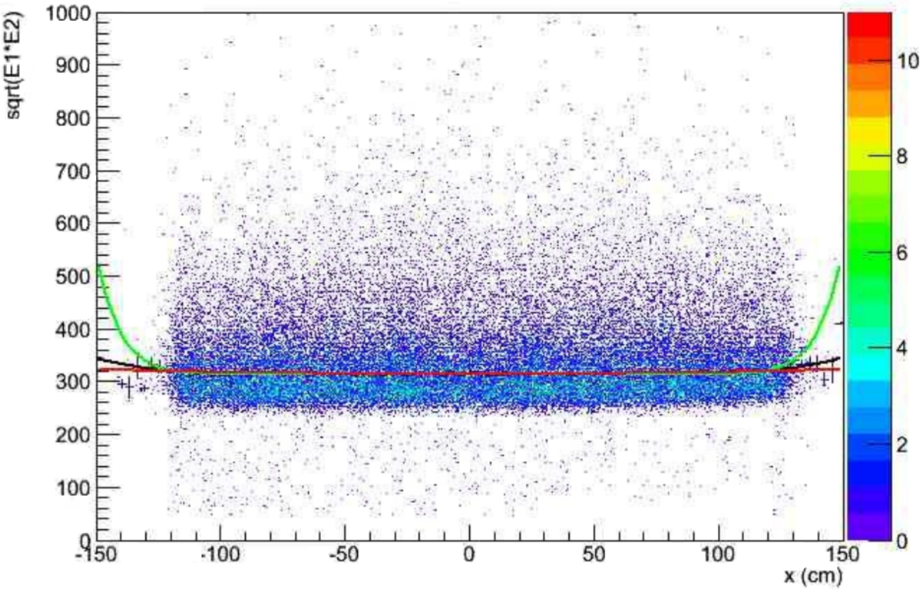

Figure 6.14: $\sqrt{E_L E_R}$ plotted as function of the position of the interaction point. If there are reflections, the smiley effect should be seen here. The effect can be seen on the fitted plots where a larger α gives rise to what looks like a smiley. There is no visible smiley effect in the experimental data.

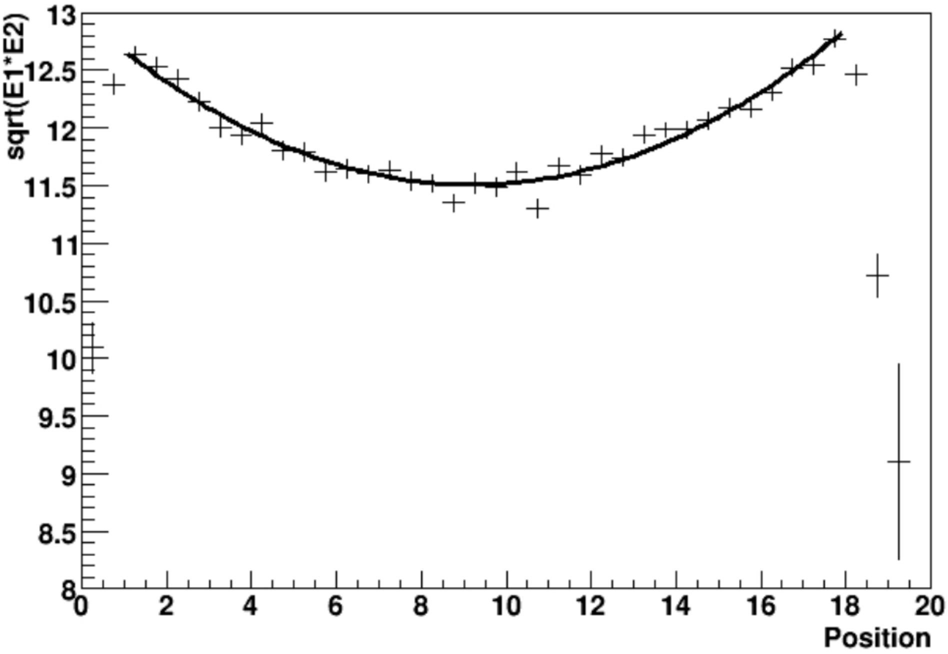

Figure 6.15: $\sqrt{E_L E_R}$ plotted as a function of position of interaction point in one of the paddles of LAND in experiment S245. An unexpected position dependence is observable. Figure from Ref. [8].

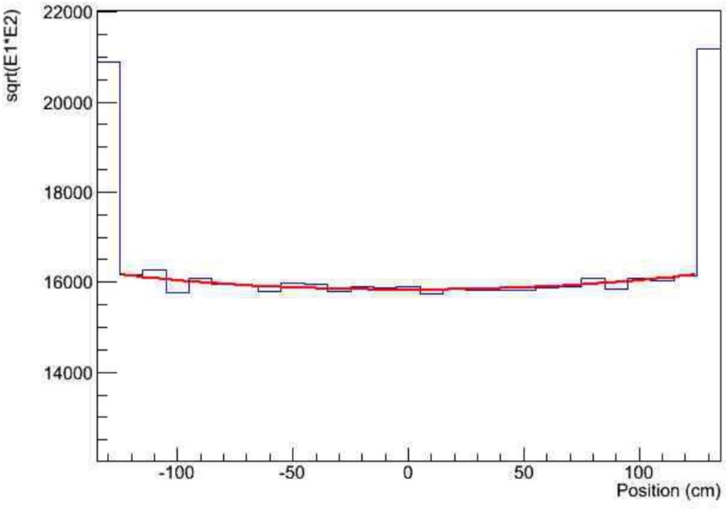

Figure 6.16: Simulations of $\sqrt{E_L E_R}$ plotted as a function of position of interaction point. The simulation show a position dependence on $\sqrt{E_L E_R}$ which arises from reflections at the ends of the bar.

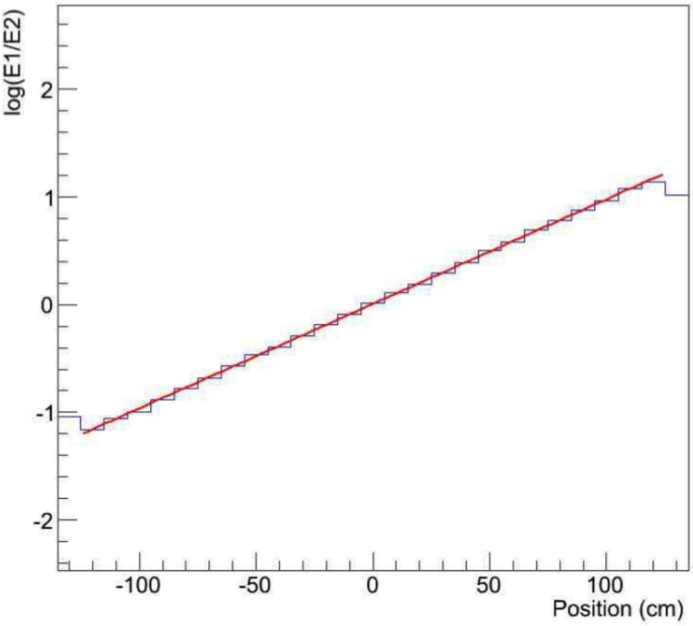

Figure 6.17: Simulations of $\ln \frac{E_L}{E_R}$ plotted as a function of position of interaction point. The slope can be determined but to evaluate the attenuation length the reflectivity constant needs to be known. From the simulations alone, the attenuation length can not be determined.

7

Discussion on the characterisation of NeuLAND bars

Having confirmed the existance of PMT non-linearity, the LED intensity and frequency were lowered so that both LED and cosmic muon measurements can be performed simultaneously. The results demonstrate that the two quantities (the measured attenuation of light intensity with LED and cosmic muons) are to some extent uncoupled. A bar can have the same measured attenuation of light intensity when measuring with an LED as the standard bar, while the results from the cosmic muon measurements may differ, see Figure 7.1. The cosmic muon response is coupled to the amount of scintillating material the bar contains as well as the material properties of the bar e.g. attenuation length and surface quality. The scintillating material creates photons when particles interact with it, a larger amount of this material present in a bar means that a larger number of photons is created when for example muons traverse it. This amount seems to vary between batches of bar deliveries. The LED measurements on the other side do not depend on the amount of scintillator in the bar. The light emitted from the LED into the bar reflects against the surfaces of the bar before reaching the PMT. These measurements therefore give a hint on the quality of the bar surfaces. Thus, when characterising the NeuLAND bars, it is important not to neglect any of these components, both the LED and cosmic muon measurements should be taken into account. The criteria for judging a bar to be sufficiently good is thus that both the cosmic muon and LED response to be above 90% of that of the standard bar.

The reflectivity constant needs to be determined in order to measure the attenuation length correctly. It was seen that the reflections originated from the light guides but the reflectivity constant could not be determined from the simulations. The latter needs to be determined by measurements using an oscilloscope and is part of future work in case there is a wish to measure the absolute value of the attenuation length in the NeuLAND bars.

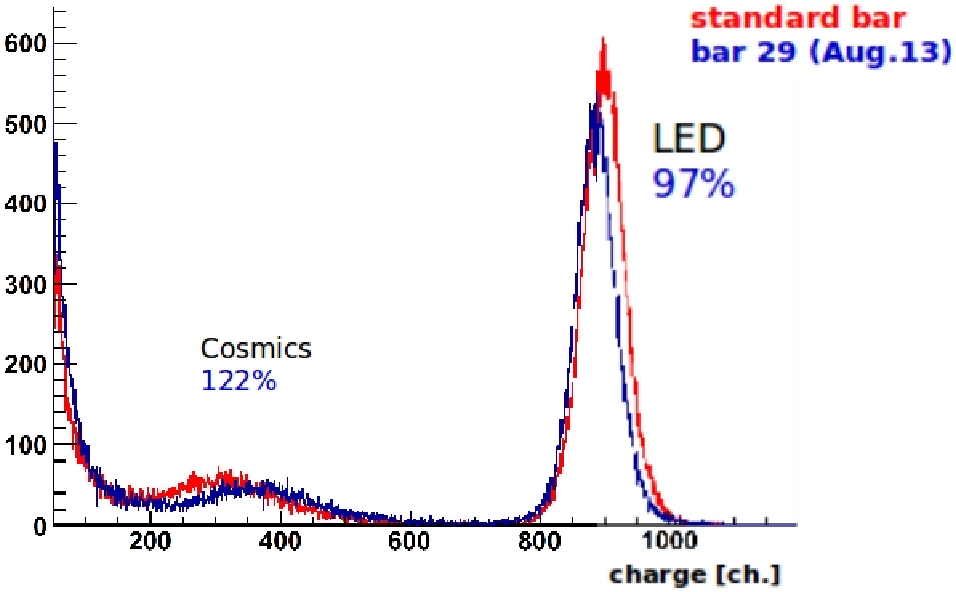

Figure 7.1: Spectrum from measurements of bar 29 (blue) and the standard bar (red). The LED pulse frequency has been lowered to allow for simultaneous LED and cosmic muon measurements. Two peaks can be noticed at channel numbers ~300 and ~900. The peak corresponding to the lower channel number is caused by photons created by cosmic muons traversing the bars while the peak at the larger channel number is caused by photons from the LED. The two values are not coupled, the value of μ_{gauss} of bar 29 is at 97% of the standard bar while the μ_{gauss} value from the cosmic muon measurement is at 122% of the standard bar.

Part III

Data analysis of S406

8

Background: Data analysis of S406

Apart from the NeuLAND bar characterisation, this thesis work includes also data analysis of experiment S406. The idea was initially to look if a *walk-effect* in the DTF detector exists, i.e. if the time measured differs depending on the amount of energy deposited in the detector. During this work, a strange phenomenon was noticed in the CXB detector setup (section 3.6). Protons seem to traverse the CXB crystal without depositing any energy in it. The proposed explanation is *crosstalk* in the electronics. This is electromagnetic interference between different channels in the electronics, where a signal in one channel gives rise to a signal in a neighbouring channel of the same electronic module. Other examples of crosstalk include crosstalk between cables when the cable carrying the signal is too close to other cables.

A notation when discussing the time-of-flight (TOF) between different detectors is introduced. To describe the TOF from detector A to detector B, the notation TOF(A,B) is used.

9

Crosstalk in the CXB crystal electronics

The CXB crystal was surrounded with six plastic scintillator detectors, see Figure 3.9. CX1 in front (between the CXB crystal and DTF), CX6 at the back and CX2-CX5 at the sides of it.

Examining time-of-flight data from experiment S406, a typical TOF spectrum between POS and DTF for protons (although there is also a possibility for deuterons to impinge on DTF, depending on the beam energy) is presented in Figure 9.1, yielding a single sharp peak (as a result from a monoenergetic beam and the quasi-elastic break-up of deuterons). The TOF(DTF,CX1) spectrum on the other hand shows an extra peak (Figure 9.2).

9.1 A closer look at time-of-flights

Examining the TOF, in both TOF(DTF,CX6) and TOF(DTF,CX1), an inconsistency can be observed. In Figure 9.3a it is seen that the lagging peak (around 7 ns) is present in both spectra with the same shape and amplitude. In other words the events corresponding to the lagging peak did not decrease in number, while the main peak did. To make sure that the lagging peak in both spectra corresponds to the same events, a cut is applied to remove the peak from TOF(DTF,CX1) (Figure 9.3b). It is seen that there are no events lagging in time recorded in the second detector in this case either, meaning that the events corresponding to the lagging peak appear in both spectra.

The lower number of counts in the spectrum at ∼2 ns suggests that protons interacted with the crystal and a part of them deposited all of their kinetic energy in the crystal. The fact that the events in the lagging peak did not, either means that the protons corresponding to these events had such a high energy that none of them were stopped in the crystal, or that they did not interact with the crystal at all, depositing no energy.

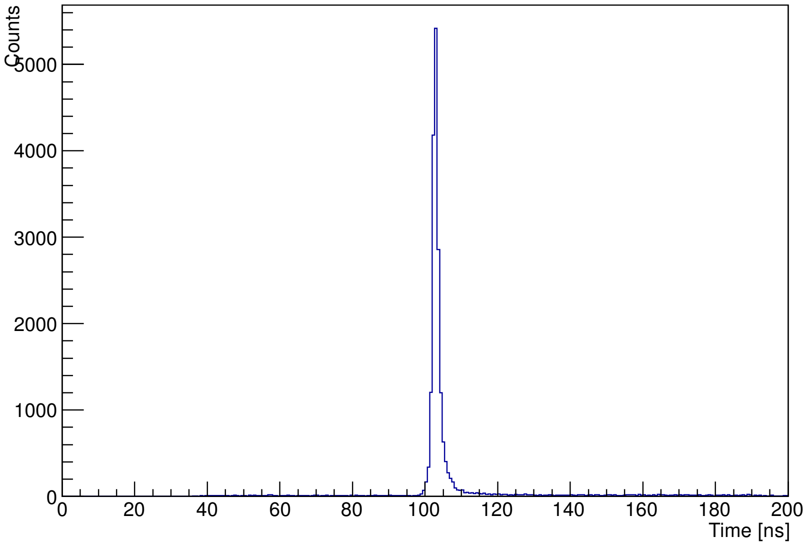

Figure 9.1: Time-of-flight spectrum for the 800 MeV/u Deuteron beam run. The time-of-flight is measured between the POS and DTF detectors.

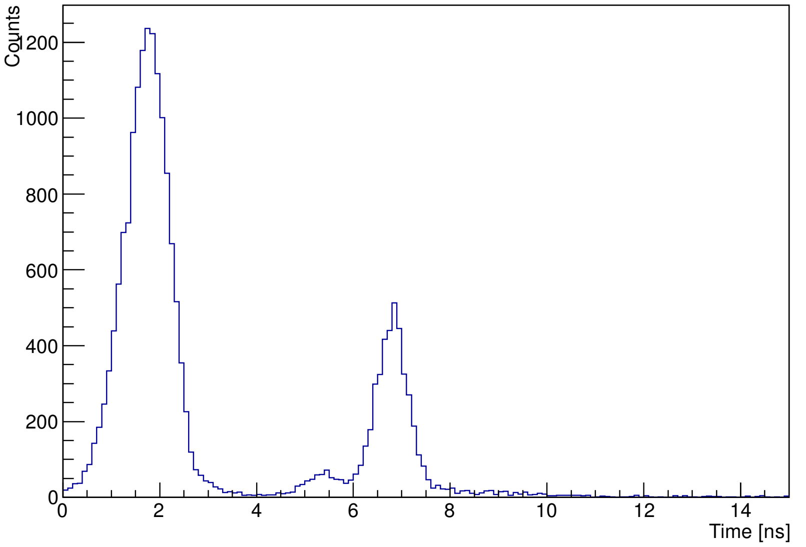

Figure 9.2: Time-of-flight spectrum for the 800 MeV/u beam measurements. The time-of-flight is measured between the DTF detector and CX1 plastic scintillator.

To find out which one of these options is the correct one, the deposited energy in the CXB crystal from the protons was investigated.

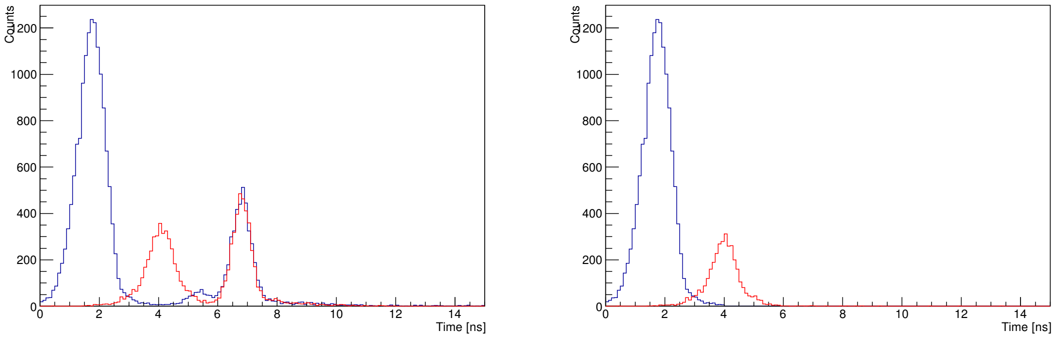

(a) **(b)**

Figure 9.3: Time-of-flight histogram from a measurement with a 800 MeV/u incident beam energy. The blue line corresponds to the TOF(DTF,CX1) and the red to TOF(DTF,CX6). The TOF(DTF,CX6) has been shifted in time so that the lagging peaks coincide. In (a) no cuts have been applied to the data, in (b) a cut was applied on the TOF to remove the lagging peak in TOF(DTF,CX1).

9.2 Deposited energy

The energy deposition in a detector is proportional to the square root of the signals obtained at the PMTs, see the second part of equation 6.2. Deposited energy plotted against the TOF in the DTF crystal is strongly correlated in time and energy because the incoming particles have (approximately) the same energy (Figure 9.4).

Using appropriate cuts, the energy signal for the different cases in the CXB crystal can be investigated as well. By plotting energy deposit against TOF(DTF,CX1) it becomes clear that the events which give rise to the extra peaks do not deposit any energy at all in the crystal (Figure 9.5) while appearing again in CX6. The conclusion is that the 'particles' traversing the crystal do not deposit any energy in the crystal, and thus do not interact with it at all. This raises some eyebrows because protons, which are charged particles, cannot pass a NaI crystal without interacting with it. A next step to investigate this observation further is to inspect how these particles interact with the DTF detector.

9.3 Interaction position at the DTF bar

Once the time differences measured in DTF are correlated to the TOF(DTF,CX1) it can be seen that, depending on the interaction position along the bar, different times

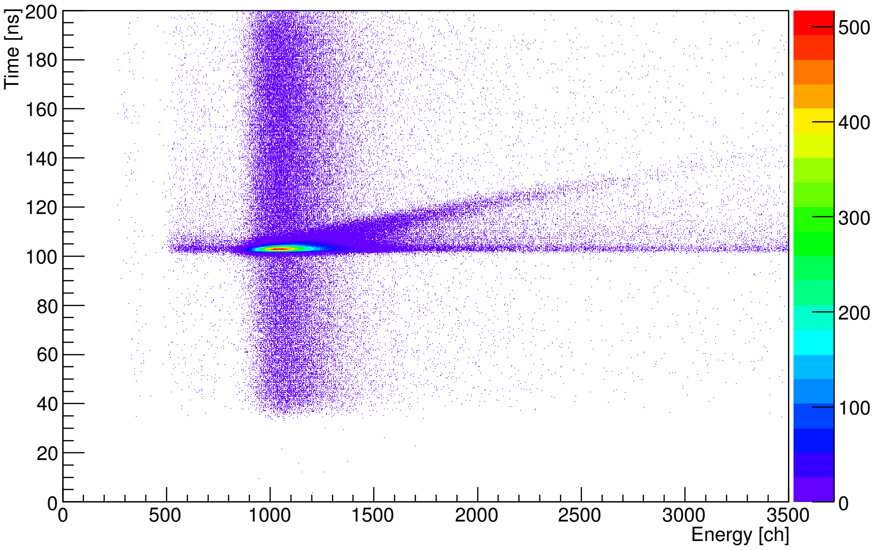

Figure 9.4: The TOF(POS,DTF) plotted against deposited energy in DTF bar 5 for the 800 MeV/u run.

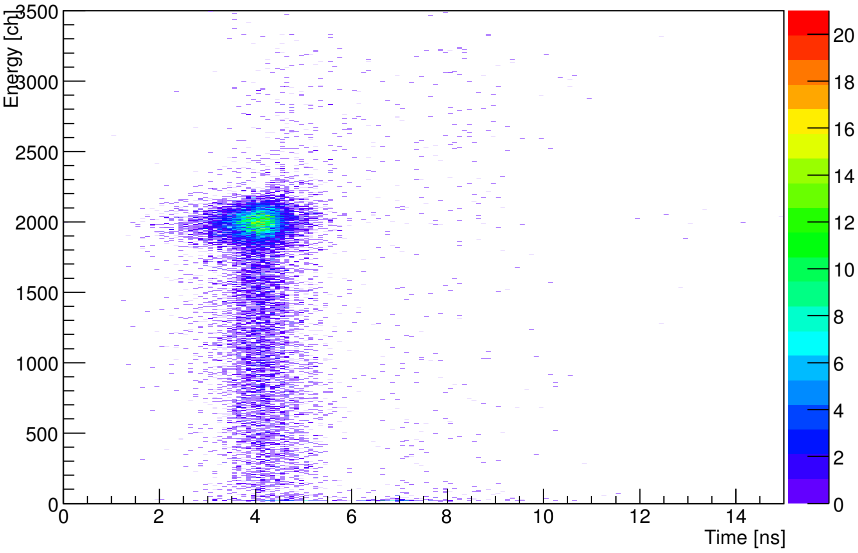

Figure 9.5: Deposited energy in CXB plotted against TOF(DTF,CX6). There is a large energy deposit at around 4 ns which corresponds to the peak around 2 ns in Figure 9.2, while no energy was measured for the lagging peak at 7 ns.

were measured in CX1 (Figure 9.6). The time difference is about 2 ns or ∼30 cm[1]. The distance between CX2 and CX3 was 28 cm. If it can be shown that the particles which impinged the DTF 15 cm above and beneath the center of the bar also impinged on the plastic scintillators CX2-CX5, it would make a strong case in favour of an explanation involving crosstalk. In that case the signals produced in CX2-CX5 would have been transferred by electromagnetic interference in the electronic channels to the channels corresponding to CX1 and CX6 within one electronic module, generating spurious events in the data. This would explain why there is no energy deposition in the crystal from these events, since the particles never traversed it.

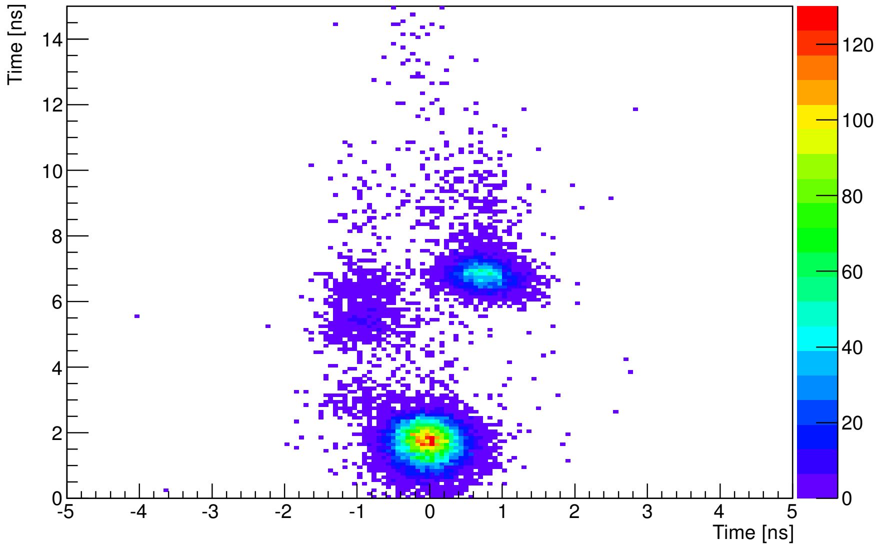

Figure 9.6: Time difference plotted against TOF(DTF,CX1). Particles which impinged the bar above or beneath the center of the bar also had recorded events in the CX1 detector, although with a 4-5 ns delay.

9.4 TOF for the different scintillators

To make sure the assumption of crosstalk is correct, there is a need to look at the plastic scintillators surrounding the crystal (CXi, i=2,3,4,5). The graphs corresponding to the correlations between TOF(DTF,CX6) and the time in CXi can be seen in Figure 9.7. It can be observed that there are indeed hits in the plastic scintillators which correspond to the time of the lagging signal (together with CX6). To ensure that these scintillator hits are indeed responsible for the lagging peak in CX6 and CX1 (through crosstalk) the

---

[1] In vacuum, light travels at a velocity of around 30 cm/ns, while in the bar this value is reduced by a factor of two, ∼15 cm/ns, see section 6.1

time difference in DTF and the TOF(DTF,CX1) may be studied (which was performed earlier) but now with cuts excluding hits on the remaining scintillators (CXi,i=2,3,4,5), see Figure 9.8. In this case all the extra peaks disappear and the result is one single peak. This clearly suggests that the effect arises from crosstalk and can be avoided in the future by connecting the cables in a way that cables from closely placed detectors are not connected next to each other.

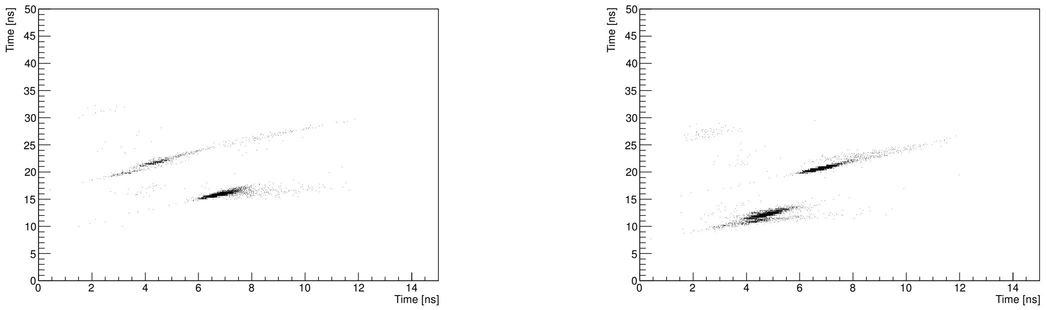

(a) TOF(DTF,CX6) vs TOF(DTF,CX2)

(b) TOF(DTF,CX6) vs TOF(DTF,CX3)

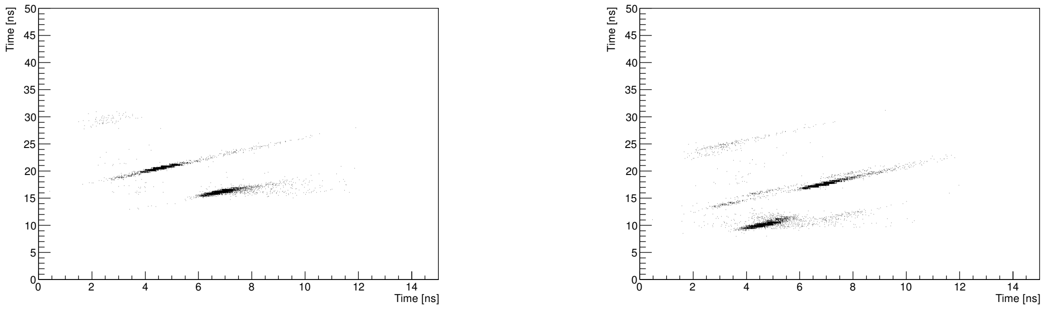

(c) TOF(DTF,CX6) vs TOF(DTF,CX4)

(d) TOF(DTF,CX6) vs TOF(DTF,CX5)

Figure 9.7: TOF(DTF,CX6) plotted as a function of TOF(DTF,CXi), where CXi stands for CX2 through CX5, for 800 AMeV beam energy. Two different peaks are seen in all four detectors. The right peak corresponds in time to the lagging peak.

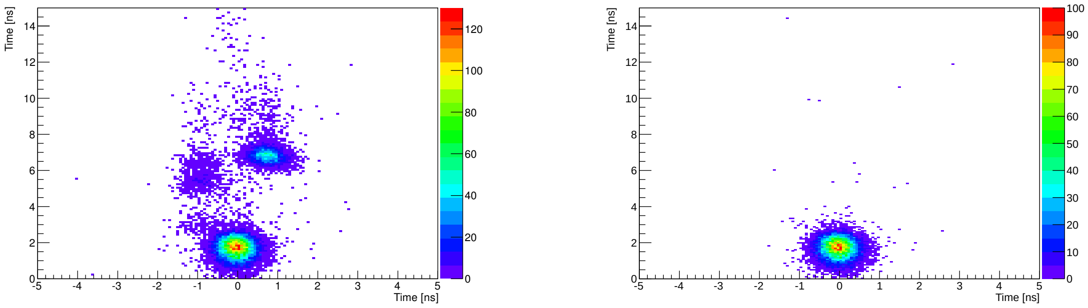

(a) **(b)**

Figure 9.8: TOF(DTF,CX1) plotted against position of hit on DTF bar 5. In (a) no cuts have been applied and in (b) cuts have been applied to remove events where the particles impinged the CX2-CX5 plastic scintillator detectors. In the latter case, the events lagging in time, TOF(DTF,CX1) also disappear.

10

The Walk Effect

In nuclear and particle physics, timing refers to measurements of very small time intervals. Examples include lifetime and time-of-flight measurements. But it is not always straighforward to conduct these measurements, often problems arise which need to be adressed.

One of these issues is the walk effect, which essentially means that there is a dependence of time measurements on signal amplitude and/or risetime. That is, for two coincident signals (A and B) at time t, with different amplitude heights, different times are measured.

There are different approaches how to address this problem. One of them is to change the timing method used in the electronics. In this introduction two common methods for timing-signal discrimination are discussed, leading edge discrimination (LED) and constant fraction discrimination (CFD) [2].

In this chapter the walk-effect in the DTF detector is discussed. An analysis of the walk-effect is of importance not only for analysis of the S406 experimental data but also for future experiments where precise time measurements are needed.

10.1 Leading Edge Discrimination (LED)

In a leading edge discriminator, when the leading edge of the signal reaches a certain absolute value, it generates a logic signal which is sent to the TDC as a start signal for the time measurement. A signal with a larger amplitude generates the logic signal earlier compared to a signal with a smaller one, leading to different timing (see Figure 10.1); this is called walk. Although LED timing is subject to problems with walk, it can still be used with good results if the amplitudes are kept within a small range. At larger differences between the amplitudes, the walk becomes a great problem and may cause fluctuations up to ±10 ns [2]. Due to its simple principle, LED is not only a faster discrimination method but LEDs are also cheaper, require less effort to set up and maintain compared to other methods, like CFD [16] [23].

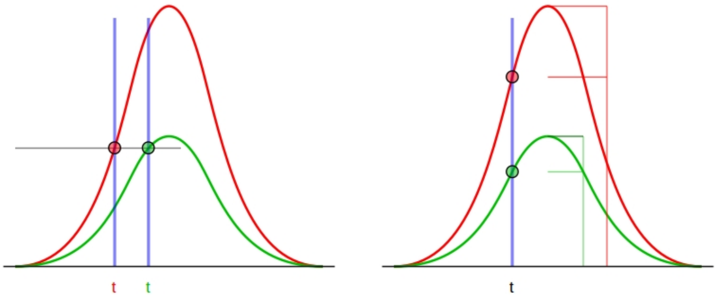

Figure 10.1: The principle of leading edge discrimination (left) and constant fraction discrimination (right). In the case of LED, the timing differs due to the different amplitudes of the signals when the triggering is based on an absolute value. In the case of CFD, which triggers on a certain constant fraction of the signal amplitude, the resulting timing is, in principle, identical in both cases, assuming that both signals have the same shape. Figure from Ref. [24]

10.2 Constant Fraction Discrimination (CFD)

Instead of discriminating at a certain absolute threshold as in LED, in a CFD a logic signal is produced at a certain fraction of the signal amplitude, which in theory should result in a walk-free timing signal, assuming that the signals have the same shape. It has also been shown empirically that there exists an optimum discrimination level that gives the best timing resolution, depending on the signal type [2].

How CFD works can easily be explained in the following steps:

- Split the incoming signal (V_a) into two, where
  - one of them is delayed by a time τ_d equal to the time needed to rise from the constant fraction level to the pulse peak.
  - the other is inverted and attenuated by a factor k to give a pulse $V_c = -kV_a$.
- Sum the two pulses, V_d and V_c, resulting in a bipolar pulse, V_{out}.
- The zero-point where the signals cancel is at a constant fraction k of the incoming signal.

Although, in theory CFD should result in a walk-free signal, there is a small walk effect in CFD as well. This is partly due to problems with setting the correct delay time for the signal and partly due to the shape of the signal. If it has an irregular shape, the constant fraction discrimination results in walk. The CFDs also differ between the models, making it hard to set up the CFDs perfectly. Different people set them up

Table 10.1: Calculated time-of-flights TOF(POS,DTF) for different beam energies using the ATIMA software.

Incoming beam energy [MeV/u]	Proton energy at DTF [MeV]	Time-of-flight [ns]
200	196.25	59.81
1000	996.56	38.06
1500	1496.78	37.24

differently. Despite this, the CFD does perform much better than the LED with respect to walk [25].

10.3 Walk effect in DTF

The importance of analysing the walk-effect in the DTF detector is, as noted earlier, not only of importance for the data analysis of experiment S406 but also the future experiments in which the detector is to be used. DTF is using a constant fraction discriminator (CFD) which in theory should not give rise to any walk. To determine this, the time-of-flight was calculated using ATIMA [11], a programme for energy loss calculations as well as extracted from the experimental data, see Table 10.1. The values obtained from the calculations were subtracted from the experimental values (which contain a constant offset). In case there is no walk present, the result should be constant, yielding the offset in the experimental data when the time difference is plotted against different beam energies. A plot of the time difference against beam energy for four different vertical bars in the DTF is seen in Figure 10.2, for each bar two cuts in the deposited energy has been performed, 1σ respectively 2σ around the mean deposited energy in both POS and the DTF bar.

The time difference observed is in the order of a couple ns (largest difference observed is around 5 ns in bar 5). This should be compared to the time-resolution of the detector which can be evaluated using equation 3.2 and the time-of-flights TOF(POS,POS++) and TOF(POS,DTF), see Figure 10.3. The time resolution for DTF bar 5 for a beam-energy of 800 MeV/u is estimated to 0.72 ± 0.015 ns, and is one order of magnitude smaller than the walk. The calculated time-of-flights is around ~30-60 ns, making the walk (~5 ns) a significant effect.

Note that the time difference is larger at lower beam energies. This is counter-intuitive since larger signals should give rise to shorter time measurements, and slower particles (which have a lower kinetic energy) deposit more energy than faster (high energy) particles. Expected is rather that the time difference should be larger at higher beam energies.

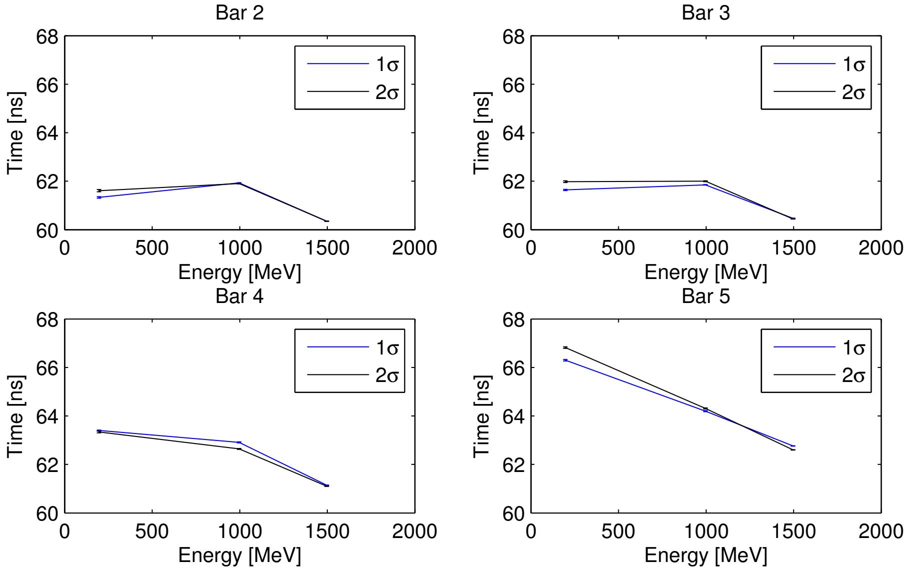

Figure 10.2: Walk curves for four of the six vertical bars in DTF. The energy depicts the incoming beam energy. The time is absolute time difference between the measured time-of-flight (with an offset) and calculated time. For each bar two cuts in the deposited energy have been performed, 1σ and 2σ around the mean deposited energy in both POS and the DTF bar respectively. Note that there exists an energy dependence on the timing, suggesting that walk exists in the DTF.

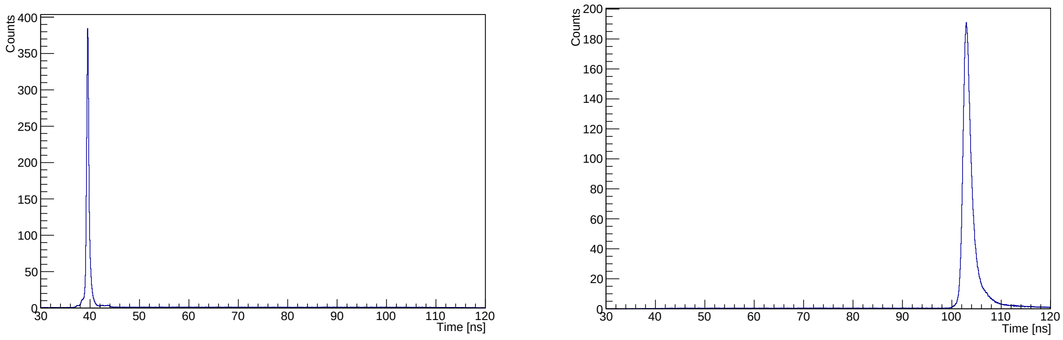

(a)

(b)

Figure 10.3: Time-of-flight histogram for a 800 MeV/u measurement for (a) TOF(POS,POS++) with a mean of 39.5 ns and a width $0.274 \pm 6.43 * 10^{-3}$ ns. (b) TOF(POS,DTF bar 5) with a mean of 103.1 ns and a width $0.749 \pm 1.25 * 10^{-2}$ ns. The DTF time-of-flight resolution is calculated with respect to the widths using equation 3.2 to be 0.72 ± 0.015 ns.

10.4 Land02 walk programme

The land02 walk programme computes the walk curves from the raw data files directly. The principle is that the time measured in the experiment is a function of the amplitude of the signal:

$$t = t_0 + f(e) \tag{10.1}$$

where t is the measured time, t_0 is the unknown 'real' time and f(e) is the amplitude (or energy) dependence. Since t_0 is unknown, f(e) can not be solved for. The assumption is that there are two neighbouring bars, both of which the particle (in whose time measurement there is interest) traverses, see Figure 10.4. In that case there are four PMTs (two on each bar) which give four unknown equations of the form of equation 10.1, one for each PMT. Because the bars are assumed to be neighbours, the real time t_0 is in all cases assumed to be approximately the same. Then equation 10.1 can be rewritten on the form:

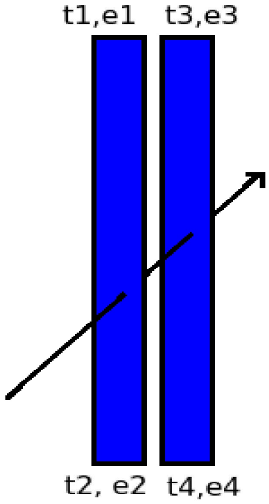

Figure 10.4: A schematic figure showing two bars and a particle passing through them. Each PMT measures a time and energy when the particle traverses the bars.

$$t_0' = \frac{(t_1 - f_1(e_1) + t_2 - f_2(e_2))}{2} + C_1 = \frac{(t_3 - f_3(e_3) + t_4 - f_4(e_4))}{2} + C_2 \tag{10.2}$$

where t_0' is the real time, t_i is the time measured in PMT i, C_i is a constant and $f_i(e_i)$ is the walk function of PMT i. Equation 10.2 is rewritten such that all the time terms end up on the left hand side and the rest on the right hand side:

$$(t_1 + t_2) - (t_3 + t_4) = f_1(e_1) + f_2(e_2) - (f_3(e_3) + f_4(e_4)) + C' \tag{10.3}$$

where C' is a constant. The t_i values are known, meaning that the only unknowns are the walk functions. To compute them, events are chosen such that for example e_i, i=2,3,4 are constant and e_1 is allowed to range over a certain number of values. Then the following equation is obtained:

$$f_1(e_1) = -(t_1 + t_2) + (t_3 + t_4) + C'(e_2,e_3,e_4) \tag{10.4}$$

and the walk function can be computed. By choosing different values of e_2,e_3 and e_4, different constants C' are obtained, giving different offsets, see Figure 10.5. The walk function is determined by a linear least squares method applied to all the walk functions obtained for a specific PMT.

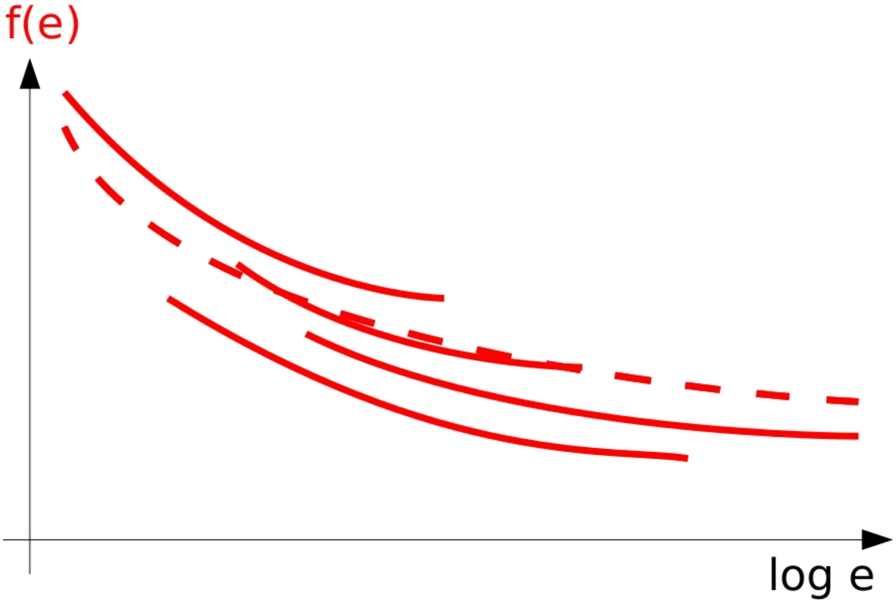

Figure 10.5: A schematic plot of a walk curve, f(e) plotted against logarithmic energy, log(e). The different filled lines corresponds to different walk curves obtained by solving equation 10.4 for different energies. They correspond to the same walk function (dotted line) but have different offset.

10.4.1 Land02 walk programme applied to DTF

The programme was applied to the DTF detector in a measurement from experiment S406 with an incident beam energy of 800 Mev/u. One of the issues with DTF with regards to the walk programme, is that the programme assumes that the bars neighbour each other, which is not the case for the horizontal bars of DTF. The walk curves of these bars can then not be trusted. The results are in Figure 10.6. The figure shows 16 walk curves for the two PMTs of the 8 bars of DTF. Each PMT has several curves ranging different energy intervals. These curves contain an offset in time and it should in principle be possible to shift the times and align them with each other. This is not the case in most of these walk curves. The problem is that the energy range covered is not large enough. To obtain better walk curves, a measurement which covers a larger range of energies should be performed.

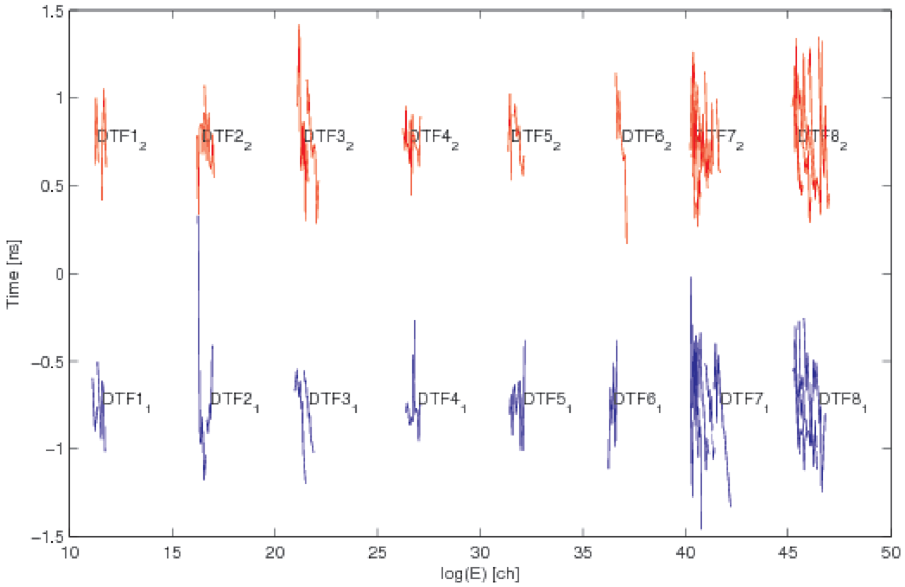

Figure 10.6: Time vs log(E). The different walk curves obtained for a 800 MeV/u measurement from experiment S406 for the DTF detector. The upper curves correspond to one PMT and the lower curves to the other PMT of a certain bar. Walk curves 1-6 correspond to vertical bars while walk curves 7-8 correspond to the two horizontal bars.

A crude model of one of the walk curves (DTF3) has been implemented to see if there is any correction to the time measurements. By approximating the walk curve to a linear function the time measurement was corrected as follows:

$$t' = t - k\ln(E) \tag{10.5}$$

where t' is the walk-corrected time and k is the slope of the walk curve (it is approximated as a linear function). The implementation did not yield any result.

10.5 POS HV dependence on time measurements

In the experiment, the HV applied to the PMTs of the POS detector was optimised and thus changed often. Thus there were many measurements performed under different conditions (different HV applied to the PMTs). To see how these changes affect the time measurements, the different time-of-flights were plotted, see Figure 10.7. The applied

HV does influence the time measurements, the difference is at most ∼1.5 ns for the measurement with an incident beam energy of 200 MeV/u.

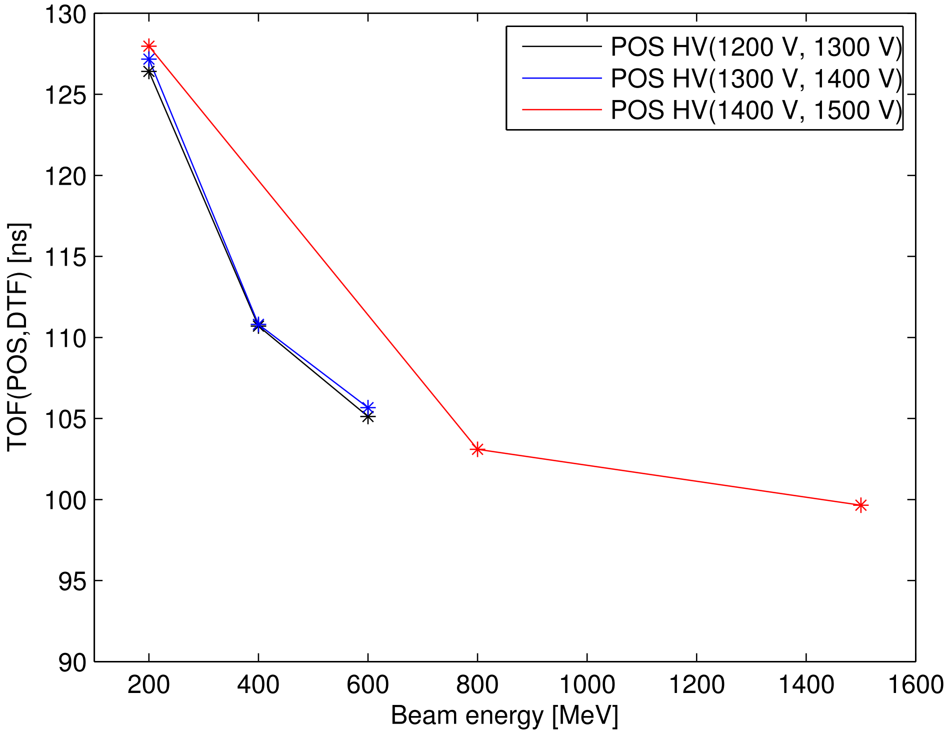

Figure 10.7: TOF(POS,DTF) plotted against incoming beam energy for different HV applied to the two PMTs of the POS detector.

11

Discussion

When discussing the cross-talk in the electronics it is important to note the way the cables are connected in the electronics. In general, detectors which lie close to each other should be connected to channels that lie far away from each other in electronic modules to avoid transference of the signal from one detector to the other, resulting in confusion and head ache.

The walk-effect was a bit tricky to measure due to the often changing circumstances between the measurements. The changes include among other frequent change of the POS HV, equipment moved around and the ALADIN current changed. This makes it difficult to extract data from measurements performed under the same condition, since there were so few of them. Despite these changes, the walk-effect has been observed by extracting time-of-flight data and by using the Land02 programme. In both cases the walk-effect is seen to be in the order of a couple ns, which should be compared to the time-resolution which is one order of magnitude smaller, while the time-of-flight is one order of magnitude larger. This is a large effect and needs to be further investigated to allow for accurate time-of-flight measurements in future experiments.

The influence of the applied HV on the POS PMTs has been investigated and a change up to $\sim$1.5 ns has been observed when changing the HV on (PMT1, PMT2) from (1200 V, 1300 V) to (1400 V, 1500 V) with a beam energy of 200 MeV/u.. This is an effect in the same order of magnitude as the walk. To be able to compare measurements performed under different POS HV conditions, further testing needs to be performed as the data collected so far does not suffice to model the behaviour.

To conclude this section, further measurements need to be performed to determine the characteristics of the walk-effect in DTF and to correct for it. The Land02 walk-programme needs to be checked to make sure it works correctly.

Bibliography

[1] Technical Report for the Design, Construction and Commissioning of NeuLAND: The High-Resolution Neutron Time-of-Flight Spectrometer for R^{3}B (2011), `http://www.fair-center.de/fileadmin/fair/experiments/NUSTAR/Pdf/TDRs/NeuLAND-TDR-Web.pdf`.

[2] W.R.Leo, 'Techniques for Nuclear and Particle Physics, A How-to Approach'. Springer-Verlag, 1987.

[3] H.T.Johansson, 'Hunting Tools Beyond the Driplines', PhD thesis, Chalmers University of Technology, 2010.

[4] R^{3}B web page, `https://www.gsi.de/work/forschung/nustarenna/kernreaktionen/activities/r3b.htm`

[5] IRFU's (Institute of Research into Fundamental laws of Universe) web site on R^{3}B, `http://irfu.cea.fr/en/Phocea/Vie_des_labos/Ast/ast_technique.php?id_ast=2108`

[6] FAIR R^{3}B web page, `http://www.fair-center.eu/public/experiment-program/nustar-physics/r3b.html`

[7] K.Boretzky, Characterization of NeuLAND prototypes and the LAND detector using fast 'monoenergetic' neutrons. `https://elog.gsi.de/S40x/120111_104612/Proposal-R3B-NeuLAND.pdf`

[8] S.Lindberg, 'Optimised Use of Detector Systems for Relativistic Radioactive Beams - How to kill a smiley and get away with it!', Master's thesis, Chalmers University of Technology, 2013.

[9] K.Boretzky *et al.*, 'Construction and Test of a Large NeuLAND Prototype Array', GSI Report 2013-1, 190- p. (2013)

[10] Private conversation with Igor Gasparic, GSI.

[11] R.Plag, 'Land02 - featuring the unofficial guide to the unofficial version of land02', `http://web-docs.gsi.de/~rplag/land02/index.php`

[12] R.Thies, 'Prototype tests and pilot experiments for the R^3B scintillator-based detetion systems', Master's thesis, Chalmers University of Technology, 2011.

[13] V.Metag *et al.*, 'The Darmstadt-Heidelberg-crystal-ball', Lecture Notes in Physics, Vol 178, 1983, pp 163-178.

[14] P.Regan, 'Post Graduate Nuclear Experimental Techniques(4NET) Course Notes'.

[15] B.Ocker, 'Kalibrierung der ALADIN-Flugzeitwand', Diploma thesis, Johann Wolfgang Goethe-Universität, 1993.

[16] Private conversation with Michael Heil, GSI.

[17] T.Axelsson *et al.*, 'Calibration detetor for Crystal Ball', Chalmers University of Technology, 2012.

[18] Christoph Caesar, Beyond the Neutron Drip-Line: Superheavy Oxygen Isotopes, PhD thesis, TU Darmstadt (2012).

[19] S.Pal *et al.*, 'Measurement of integrated flux of cosmic ray muons at sea level using the INO-ICAL prototype detector', Journal of Cosmology and Astroparticle Physics, 2012

[20] J.Kempa, M.Brancus, 'Zenith angle distributions of cosmic ray muons', Nuclear Physics B (Proc. Suppl.), vol. 122, pp. 279-281, 2006.

[21] 'Gamma Background', `http://pro.ganil-spiral2.eu/users-guide/gamma-background/background-spectra/at_download/file`

[22] Geant4 collaboration, Agostinelli, S. et al. (2003). 'Geant 4 - a simulation toolkit, Nuclear Instrument and Methods in Physics Research A', vol. 506, pp. 250-303.

[23] Private conversation with Andreas Heinz, Chalmers University of Technology.

[24] 'Constant Fraction Discriminator', `http://en.wikipedia.org/wiki/Constant_fraction_discriminator`.

[25] Private conversation with A. Heinz, H.Johansson and T.Nilsson, Chalmers University of Technology.